

REVIEW ARTICLE | OCTOBER 14 2020

# Chip-scale nonlinear photonics for quantum light generation

SCI F

Special Collection: **Quantum Photonics**

Galan Moody ; Lin Chang; Trevor J. Steiner ; John E. Bowers

Check for updates

AVS Quantum Sci. 2, 041702 (2020)

<https://doi.org/10.1116/5.0020684>

CHORUS

View  
OnlineExport  
Citation

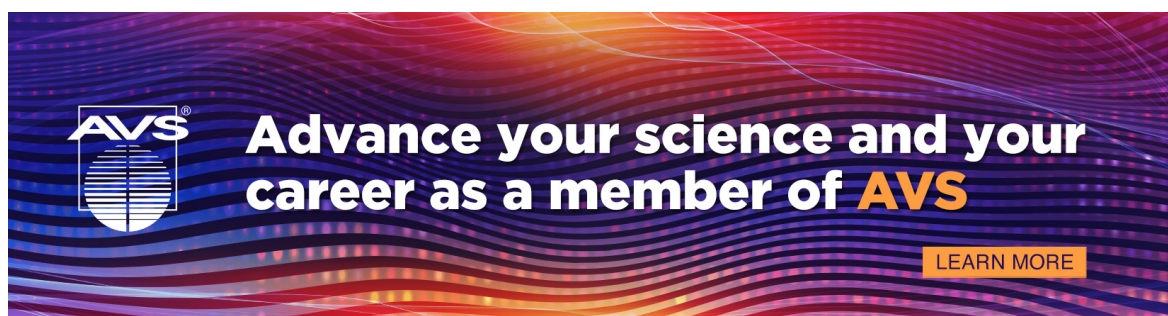
## Articles You May Be Interested In

On-chip heralded single photon sources

AVS Quantum Sci. (October 2020)

Photonic quantum metrology

AVS Quantum Sci. (June 2020)



# Chip-scale nonlinear photonics for quantum light generation

SCI F

Cite as: AVS Quantum Sci. 2, 041702 (2020); doi: 10.1116/5.0020684

Submitted: 2 July 2020 · Accepted: 17 September 2020 ·

Published Online: 14 October 2020



View Online



Export Citation



CrossMark

Galan Moody,<sup>1</sup> Lin Chang,<sup>1</sup> Trevor J. Steiner,<sup>2</sup> and John E. Bowers<sup>1,2</sup>

## AFFILIATIONS

<sup>1</sup>Electrical and Computer Engineering Department, University of California, Santa Barbara, California 93106, USA<sup>2</sup>Materials Department, University of California, Santa Barbara, California 93106, USA

## ABSTRACT

Nonclassical states of light are an essential resource for many emerging quantum technologies and applications ranging from information processing, encrypted communications, and networking to sensing, metrology, and imaging. Nonlinear optical processes in solid-state materials are widely used for generating quantum light, including single photons, entangled-photon pairs, and quadrature-squeezed states. Recent advances in nonlinear photonics have enabled the functionality of benchtop nonlinear instruments to be scaled down to a single chip without sacrificing efficiency or degrading the key performance metrics. The dramatic improvement in the size, weight, power, cost, and stability enabled by photonic integrated circuits has been essential for enabling the chip-scale generation, manipulation, and detection of quantum light at a steadily increasing degree of complexity and scale. Within the last decade, the authors have seen the progression from few-component photonic circuits operating on two photons to arrays of 18 identical heralded single-photon sources and reconfigurable devices operating with more than 650 components for multidimensional entanglement and arbitrary two-photon quantum gates. In this review, the authors summarize the history and recent key technological developments of chip-scale nonlinear quantum light generation based on integrated nonlinear photonics, recent advances in heterogeneous integrated methods, and approaches for system-level integration and demonstrated applications.

© 2020 Author(s). All article content, except where otherwise noted, is licensed under a Creative Commons Attribution (CC BY) license (<http://creativecommons.org/licenses/by/4.0/>). <https://doi.org/10.1116/5.0020684>

## TABLE OF CONTENTS

I. INTRODUCTION .....	1
II. QUANTUM LIGHT GENERATION .....	3
A. Nonlinear material platforms .....	4
1. Silicon (Si) .....	5
2. Silicon nitride (SiN) .....	5
3. Lithium niobate (LN) .....	5
4. III-V semiconductors .....	6
B. Heralded single-photon generation .....	7
C. Entangled-pair generation .....	8
D. Squeezed light .....	10
III. QUANTUM FREQUENCY TRANSLATION AND STATE MANIPULATION .....	12
IV. SYSTEM-LEVEL INTEGRATION AND APPLICATIONS .....	14
V. OUTLOOK .....	14

### I. INTRODUCTION

A photon is an ideal, low-noise carrier of quantum information.<sup>1</sup> Unlike matter-based quantum systems that decohere due to

interactions with their environment, photons maintain a high degree of coherence without the need for an ultra-high vacuum or millikelvin operating temperature, providing practical advantages for translating quantum photonic device concepts into application-ready technologies. Today, the most widely used approach for generating quantum states of light relies on optical conversion processes in nonlinear materials. For over two decades, the workhorse for generating single and entangled-photon pairs has been spontaneous parametric down conversion (SPDC), a  $\chi^{(2)}$  nonlinear process in which a pump photon is destroyed to create two correlated photons traditionally called the signal and idler.<sup>2–4</sup> A similar process in  $\chi^{(3)}$  nonlinear materials, spontaneous four wave mixing (SFWM), can convert two pump photons to create a pair of entangled photons, providing additional flexibility for tuning the signal and idler photon energies.<sup>5,6</sup> Both SPDC and SFWM are utilized for the generation of squeezed light with amplitude or phase noise below the standard quantum limit,<sup>7</sup> high-efficiency heralded single photons,<sup>8</sup> and entangled photon pairs.<sup>9–11</sup>

In contrast to quantum light sources based on single quantum emitters,<sup>12,13</sup> the appeal of SPDC and SFWM is their ability to operate at room temperature, the extremely high quality of photons produced, and the experimental simplicity and inexpensive cost of operation.

However, the efficiency of SPDC and SFWM is typically limited to  $\sim 10^{-5}$  pairs per pump photon in order to avoid the production of high photon-number states, although this has been improved in recent years through multiplexing.<sup>14,15</sup> Despite the low efficiency, photons can be produced with near unity indistinguishability, purity, and entanglement fidelity at near GHz pair generation rates,<sup>16</sup> making these sources appealing for a wide range of quantum information applications including secure communications,<sup>17</sup> information processing,<sup>18</sup> sensing,<sup>19</sup> metrology,<sup>20,21</sup> and foundational tests of quantum mechanics.<sup>22,23</sup>

While atomic sources of single and entangled photons have been available for over 50 years,<sup>24,25</sup> it was not until 1995 that a high-quality, intense source of polarization-entangled photon pairs became available with table-top type-II SPDC, which enabled the production of all four EPR-Bell states.<sup>9</sup> Shortly afterward, chip-scale SPDC and SFWM were realized in a variety of material systems, including waveguides fabricated in periodically poled lithium niobate (PPLN), silicon-on-insulator (SOI), AlGaAs, and chalcogenides. The monolithic integration of optical elements onto a single semiconductor chip provides several advantages that are discussed throughout this review. These include suppression of phase fluctuations and other sources of noise and decoherence, the compactness required to build complex quantum photonic networks that would be impossibly large with traditional table-top optics, and an increase in system-level efficiency that ultimately impacts information processing and communication rates.

Compared to well-established quantum platforms based on superconducting circuits and trapped ions, where operations on

quantum bits (qubits) were first implemented nearly three decades ago,<sup>26</sup> encoding and transmitting quantum information with light using quantum photonic integrated circuits (QPICs) is relatively new. A landmark result for information processing with photons was the demonstration of the first integrated quantum photonic logic gate in 2008.<sup>27</sup> Yet, despite the novelty of QPICs, in the last decade, we have seen remarkable advances in materials growth and nanofabrication techniques primarily due to the prolific existing photonics infrastructure for classical telecommunications and the commercially available tools made accessible by the silicon CMOS industry. In just under 10 years, state-of-the-art QPICs have progressed from two-photon quantum interference experiments using Hong-Ou-Mandel interferometer chips in 2012<sup>28</sup> to fully configurable circuits with over 650 components enabling multidimensional entanglement and universal two-qubit entangling operations.<sup>29–31</sup> Such technological advances pave the way for all-on-chip quantum photonics with exciting prospects for quantum information science and emerging technologies, as illustrated in Fig. 1.

With this rapid and sustained progress in the chip-scale generation, manipulation, and detection of quantum light with nonlinear photonics, new challenges and opportunities arise. Here, we review the recent developments and applications of nonlinear quantum photonics with a focus on quantum light generation. We first review and compare the nonlinear material platforms and the microfabrication techniques that have led to ultra-low material absorption and waveguide propagation loss, ultra-high microresonator quality factors, and

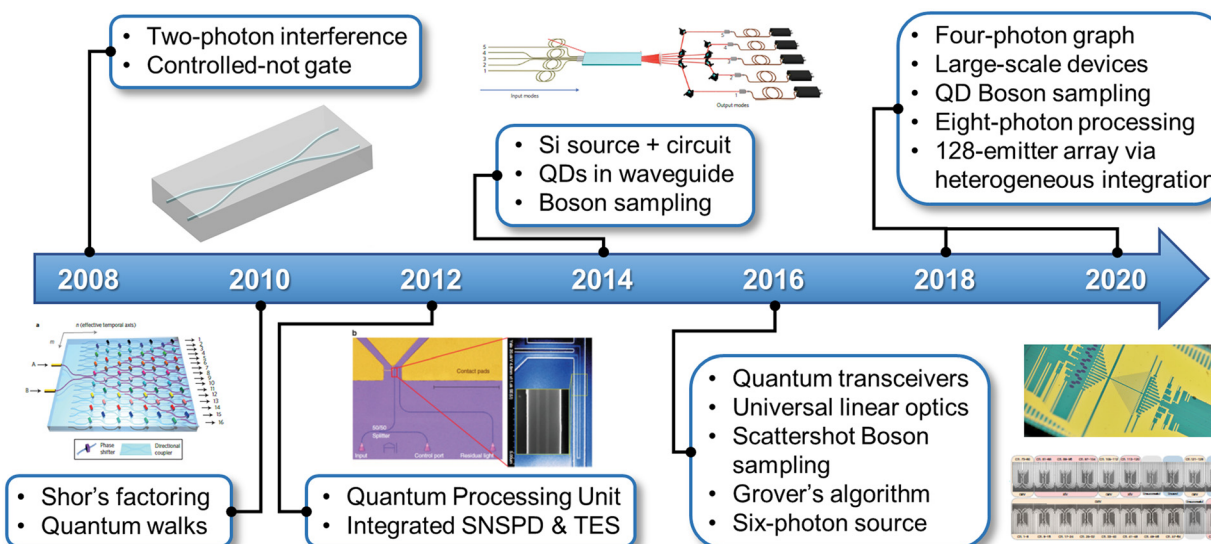


**Fig. 1.** Key milestones for integrated quantum photonics in the past decade: on-chip two-photon interference and integrated controlled not (CNOT) gate (Ref. 27); tests of Shor's algorithm (Ref. 32); quantum walks with correlated photons (Ref. 33); reprogrammable quantum processing unit (Ref. 34); waveguide-integrated single- and phonon-number resolving detectors (Ref. 35); integration of silicon probabilistic sources with circuits (Ref. 28); efficient quantum dot source coupled to a waveguide (Ref. 36); demonstration of Boson sampling with photons (Refs. 37–41); quantum transceivers for chip-to-chip quantum key distribution (QKD) (Refs. 17 and 42); integrated chip for universal linear optics (Ref. 43); scattershot Boson sampling (Ref. 44); tests of Grover's algorithm (Ref. 45); on-chip integration of six photon sources (Ref. 46); demonstration of four-photon graph states (Ref. 47); on-chip integration of eight photon sources (Ref. 48); large-scale integration of 670 components in silicon (Ref. 29); and array of 128 waveguide-integrated quantum emitters (Ref. 49). The figures (in chronological order) are reproduced with permission from Politi *et al.*, *Science* **320**, 646 (2008). Copyright 2008 The American Association for the Advancement of Science; reproduced with permission from Crespi *et al.*, *Nat. Photonics* **7**, 545 (2013). Copyright 2013 Springer Nature; reproduced with permission from Pernice *et al.*, *Nat. Commun.* **3**, 1325 (2012). Copyright 2012 Springer Nature; reproduced with permission from Crespi *et al.*, *Nat. Photonics* **7**, 545 (2013). Copyright 2013 Springer Nature; and reproduced with permission from Wan *et al.*, *Nature* **583**, 226 (2020). Copyright 2020 Springer Nature and reproduced with permission from Wang *et al.*, *Science* **360**, 285 (2018). Copyright 2018 The American Association for the Advancement of Science.

improved photon-pair brightness. We then focus on methods for chip-scale generation of three types of technologically relevant quantum states of light, namely, heralded single-photons, entangled-photon pairs, and squeezed states. We next present the state-of-the-art for nonlinear quantum frequency conversion spanning the visible and telecommunication wavelength domains. Finally, we discuss methods for system-level integration of quantum light sources, reconfigurable circuits, and single-photon detectors, the related applications including chip-scale quantum communications and computing, and the challenges and opportunities for realizing large-scale quantum photonic circuits.

## II. QUANTUM LIGHT GENERATION

Chip-scale quantum light sources fall into two classes: deterministic sources based on single-quantum emitters, such as self-assembled quantum dots (QDs), and probabilistic sources based on SPDC and SFWM. While SPDC sources are traditionally considered state-of-the-art for heralded single and entangled-photon generation, in the last few years, advances in III-V microfabrication techniques have produced high-quality QD-based sources for off-chip quantum information applications, as demonstrated by quantum key distribution<sup>50</sup> and 20-photon, 60-mode Boson sampling;<sup>51</sup> however, the primary drawbacks of QDs are the lack of control over their spatial and spectral properties, challenges with efficient coupling of emission on chip, and cryogenic operating temperature. SPDC and SFWM sources provide

significant advantages in this regard, with arrays of up to 18 indistinguishable heralded single-photon sources monolithically integrated on a silicon photonic chip.<sup>46</sup>

**Figure 2** summarizes the key concepts of nonlinear photon-pair generation. For SPDC, a  $\chi^{(2)}$  nonlinear process, a single pump photon of frequency  $\omega_p$  is annihilated, producing a pair of signal and idler photons of frequencies  $\omega_s$  and  $\omega_i$ , respectively, where  $\omega_s + \omega_i = \omega_p$ . Likewise, SFWM, a  $\chi^{(3)}$  nonlinear process, produces photon pairs through the annihilation of two pump photons while conserving energy and momentum, i.e.,  $\omega_s + \omega_i = 2\omega_p$ . The key difference is that SPDC tends to be more efficient owing to the larger  $\chi^{(2)}$  nonlinearity; however, SFWM also allows for quasi-degenerate or degenerate pump, signal, and idler photon frequencies, which has advantages for relaxed dispersion engineering requirements in photonic waveguides and resonators. Two methods for generating photon pairs, shown in Fig. 2(b), are linear or spiral waveguides and microring resonators. Waveguides can produce photon pairs efficiently with periodic poling<sup>4,52</sup> or geometry tailoring,<sup>53</sup> which enable phase matching between the pump, signal, and idler photons over a longer propagation distance; however, these structures typically require millimeter- or centimeter-long waveguides to generate appreciable signal and idler photon flux. Microresonators are advantageous in this regard, as the longer cavity lifetime enables efficient pair generation in micrometer-scale devices, which also mitigates the influence of fabrication nonuniformity on the phase-matching condition.

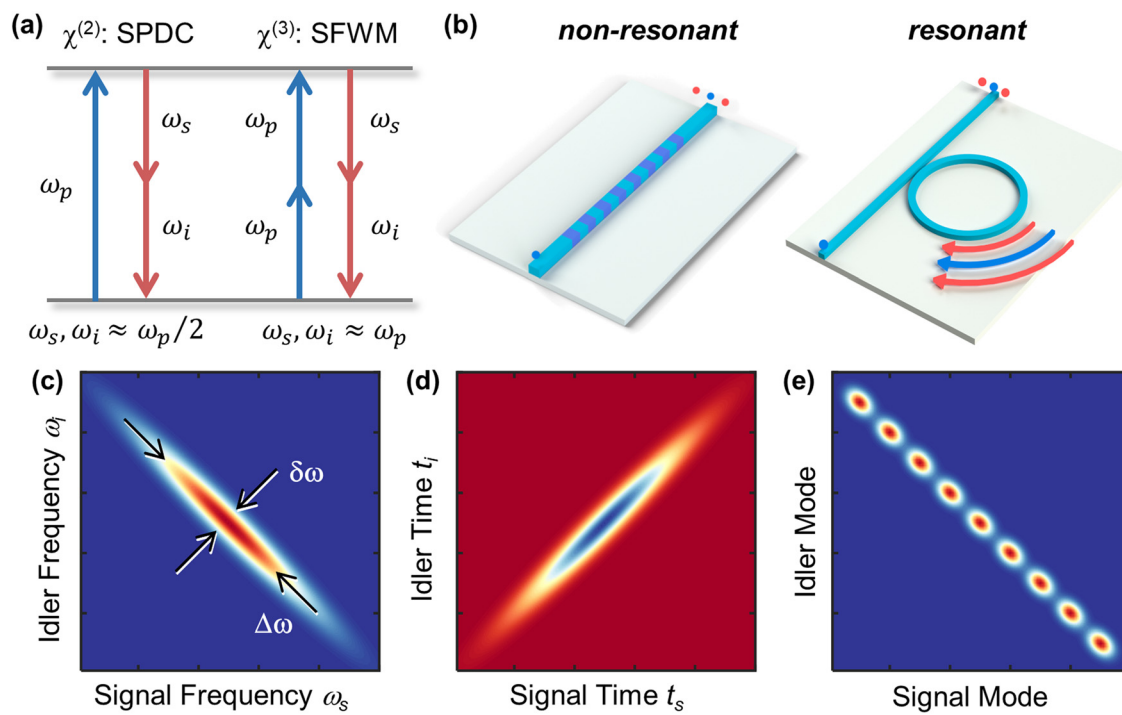


**Fig. 2.** (a) Quantum light generation with integrated nonlinear photonics relies on  $\chi^{(2)}$  (spontaneous parametric down-conversion) or  $\chi^{(3)}$  (spontaneous four-wave mixing) processes in which one or two pump photons ( $\omega_p$ ) are converted into correlated signal ( $\omega_s$ ) and idler ( $\omega_i$ ) photons, respectively. (b) Efficient frequency conversion requires energy conservation and phase matching between all three photon frequencies, which are achieved through dispersion engineering of nonresonant linear waveguides (left) and resonant microresonator structures (right). (c) and (d) Examples of joint spectral and temporal intensities exhibiting signal-idler correlations for nonresonant sources. (e) For microresonator sources, the joint spectral intensity is no longer continuous and features a series of peaks separated by the resonator free-spectral range.

Under the appropriate conditions, these devices generate a two-photon state with a small probability of producing higher photon-number states. In this case, the bi-photon state  $|1\rangle_s|1\rangle_i$  generated through SFWM, for example, is given by

$$|\psi\rangle \propto \iint \Theta(\omega_s, \omega_i) \Psi(\omega_s, \omega_i) d\omega_s d\omega_i |1\rangle_s |1\rangle_i, \quad (1)$$

where  $\Theta$  is the spectral envelope of the pump (typically considered Gaussian) and  $\Psi(\omega_s, \omega_i) = \varphi_{pm}(\omega_s, \omega_i) T(\omega_s) T(\omega_i)$  is determined by the phase-matching function  $\varphi_{pm}$  and the amplitude transmission function ( $T$ ) of the device. Conventionally,  $\varphi_{pm} = \text{sinc}(\Delta k L)$ , where  $\Delta k = 2k_p - k_s - k_i$  is the phase matching function in terms of wavenumbers  $k$  and  $L$  is the propagation length. The joint spectral intensity (JSI) is given by the magnitude squared of the joint spectral amplitude, defined as  $\Theta(\omega_s, \omega_i) \times \Psi(\omega_s, \omega_i)$  in Eq. (1). In any device geometry, the shape of the JSI, which can be measured using a variety of methods,<sup>54</sup> is determined by energy conservation and phase-matching requirements through  $\Theta$ ,  $\varphi_{pm}$ , and  $T$ . The JSI is widely used to characterize and distinguish between different bi-photon states and to quantify entanglement.<sup>55</sup> An example of a correlated bi-photon JSI is shown in Fig. 2(c). The width along the diagonal (short axis) is given by the pump photon bandwidth  $\delta\omega$ , while the length along the antidiagonal (long axis) is determined by the lesser of the spectral bandwidth of the phase-matching function  $\varphi_{pm}$  or the transmission windows  $T$ . Figure 2(d) shows the equivalent joint temporal intensity with strong correlation in the signal and idler photon generation times. For nonresonant devices, the JSI is continuous as shown in Fig. 2(c). For resonant structures,

the JSI breaks into discrete spectral resonances separated by the resonator free spectral range, as shown in Fig. 2(e).

An important metric of a bi-photon state is its separability, which can be quantified by calculating the Schmidt number,  $K$ , which represents the number of orthogonal eigenmodes of the magnitude of the joint spectral amplitude.<sup>56,57</sup> The Schmidt number can be directly determined by the square root of the JSI under the assumption of a constant spectral phase. This formalism is important for quantum information and communications, as the Schmidt number is equivalent to the Shannon number that describes the number of independent channels between a source and the receiver.<sup>58</sup> The Schmidt number can take on a range of values: for a fully separable bi-photon state in which the signal and idler photon frequencies are uncorrelated (unentangled),  $K = 1$ . On the other hand, spectral correlations spanning infinite bandwidths correspond to  $K = \infty$ . The JSIs in Fig. 2 are shown for a  $K$  value between these two extremes, similar to a maximally polarization-entangled state ( $K = 2$ ). In Sec. III, we discuss methods for manipulating the JSI without the need for spectral filtering that reduces photon flux.

### A. Nonlinear material platforms

The developments of photonic material platforms over the last decade have opened up many new opportunities for on-chip nonlinear applications.<sup>59</sup> Particularly, the significant reduction in waveguide propagation loss due to advances in material growth, defect passivation techniques, and microfabrication technologies has expanded the possible material systems capable of implementing efficient nonlinear processes, several of which are shown in Fig. 3. Based on these

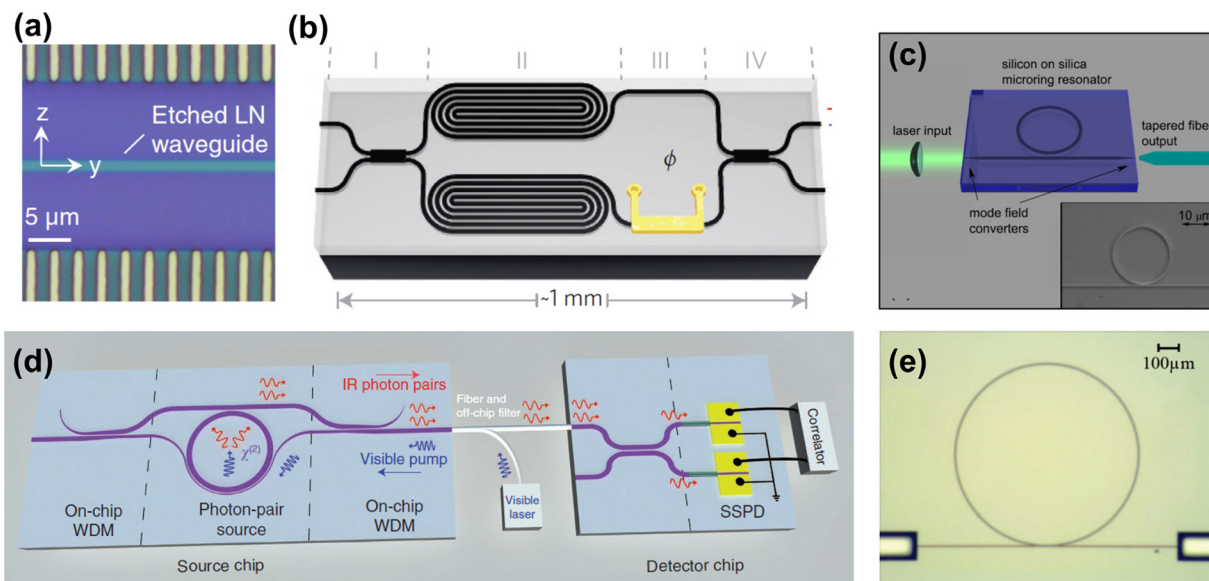


**Fig. 3.** Examples of various SPDC- and SFWM-integrated photonic sources based on linear and spiral waveguides in (a) thin-film lithium niobate (Ref. 52) and (b) silicon on silica (Ref. 31), respectively, and microresonators in (c) silicon on silica (Ref. 143), (d) aluminum nitride on silica (Ref. 94), and (e) silicon nitride on silica (Ref. 147). Panel (a) is reproduced with permission from Zhao *et al.*, Phys. Rev. Lett. **124**, 163603 (2020). Copyright 2020 American Physical Society, licensed under a Creative Commons Attribution 2.0 International License. Panel (b) is reproduced with permission from Silverstone *et al.*, Photonics **8**, 104 (2014). Copyright 2014 Springer Nature. Panel (c) is reproduced with permission from Grassani *et al.*, Optica **2**, 88 (2015). Copyright 2015 The Optical Society. Panel (d) is reproduced with permission from Guo *et al.*, Light **6**, e16249 (2017). Copyright 2017 Springer Nature. Panel (e) is reproduced with permission from Imanry *et al.*, Opt. Express **26**, 1825 (2018). Copyright 2018 Authors, licensed under the terms of the OSA Open Access Publishing Agreement.

high-performing nonlinear platforms, quantum photonic devices and system-level demonstrations have been realized. In this section, we will review the commonly used nonlinear materials and platforms in QPICs.

### 1. Silicon (Si)

The previous decade has witnessed an explosive growth in silicon photonics, which has been widely regarded as the key material system for high-speed classical and quantum telecommunications.<sup>60</sup> Silicon-on-insulator (SOI) is the central platform upon which many essential optical components are built, including Mach-Zehnder Interferometers (MZIs), delay lines, optical modulators, tunable filters, and nonlinear photon sources.<sup>61,62</sup> Besides the ubiquitous influence in classical photonic integrated circuits to date, SOI-based technologies are also responsible for rapid advances in integrated quantum photonic applications,<sup>29,30</sup> at least partially due to the existing silicon foundry infrastructure.

There are several advantages of using SOI waveguides for generating quantum light on a chip. First, Si features high  $\chi^{(3)}$  nonlinear coefficients for efficient SFWM processes.<sup>63</sup> Tight modal confinement within the waveguide due to the high refractive index contrast between Si and the  $\text{SiO}_2$  cladding serves two purposes: it enhances the efficiency of frequency conversion due to the modal overlap between pump, signal, and idler frequencies, and the geometry can be tailored to engineer the dispersion, which facilitates optimal phase matching. Most importantly, since SOI fabrication leverages the reliability, precision, and scalability of the CMOS foundry process, it leads to a high yield and reproducible technology. This facilitates the fabrication of QPICs that require a large number of photonic components in order to realize versatile and reconfigurable operations for generating, manipulating, and detecting quantum light.

The material properties of Si also lead to several limitations for QPICs. Besides the well-known fact that Si is not an efficient photon emitter due to its indirect bandgap,<sup>60</sup> it also suffers from high nonlinear losses primarily due to two photon absorption (TPA) and the induced free carrier absorption (FCA) at telecommunication wavelengths.<sup>64</sup> These place strict bounds on the power density inside the waveguide, especially for the pump light. Moreover, the absence of an electro-optic (EO) effect due to the centrosymmetric crystalline structure leads to challenges in efficient tuning. As a result, most of the demonstrations so far have to rely on thermal tuning, which is rather slow and particularly difficult at cryogenic temperature, currently preventing the integration of state-of-the-art superconducting single-photon detectors.<sup>65–67</sup> To address this problem, a PN-junction electro-optic Si modulator that harnesses carrier-induced effects for phase tuning<sup>68</sup> has been developed, but doping also introduces a higher loss due to FCA.

### 2. Silicon nitride (SiN)

SiN is another CMOS-compatible material with great promise for QPICs. Compared to the SOI platform, SiN exhibits lower material loss, a larger optical bandgap producing a broader material transparency window ranging from UV to mid-IR, and a smaller thermo-optic coefficient. These features make SiN particularly suitable for building passive circuits in QPICs with high yield, high stability, and low waveguide propagation loss.

Over the last few years, significant progress has been made in the developments of SiN photonic platforms, driven by the motivation of nonlinear applications, particularly Kerr frequency combs through SFWM. Recent advances in fabrication techniques have provided access to the anomalous group velocity regime for generation of bright soliton microcombs with a sufficient material thickness, circumventing the problems associated with high tensile stress of SiN.<sup>69</sup> To date, this type of waveguide exhibits propagation loss below 1 dB/m, corresponding to a microring resonator quality factor  $Q$  greater than  $3.0 \times 10^7$ .<sup>70,71</sup> Such high  $Q$  can dramatically enhance the optical field intensity inside the resonator, thereby enhancing the nonlinear conversion processes.

SiN microring resonators are excellent candidates for quantum light generation on chip when pumping the resonator below the threshold of parametric oscillation. In contrast to SOI platforms, the low loss of SiN is especially important for scaling, where a large number of photonic components need to be cascaded for QPICs. Moreover, the broad transparency window of SiN waveguides also supports quantum applications at visible wavelengths, where most of the atomic transitions occur. As such, this platform has been developed for compact control beams for atom and ion trapping experiments both on- and off-chip.<sup>72</sup> By applying proper dispersion engineering, entangled-photon pair generation and quantum spectral translation between visible and telecommunication wavelengths have been demonstrated based on SiN resonators,<sup>73,74</sup> providing a powerful tool for linking different quantum systems for a variety of applications in networking and sensing.

Several challenges remain that inhibit the widespread use of SiN in QPICs. First, the absolute Kerr coefficient of the material is relatively low compared to other commonly used materials (see Table I), which leads to a poor efficiency when using nonresonant waveguides for quantum light generation. Similar to Si, SiN does not exhibit a  $\chi^{(2)}$  nonlinearity, limiting the scope of potential applications and device configurations. Moreover, the thermo-optic coefficient of SiN is one order of magnitude smaller than Si.<sup>75</sup> Although this improves the thermal stability of the chip, thermo-optic tuning requires significantly more electrical power, which leads to thermal crosstalk between devices.

### 3. Lithium niobate (LN)

LN has been widely used for decades as an important nonlinear optical material for high-speed modulators due to the large electro-optic effect (EO) and the second order nonlinearity.<sup>76</sup> Over the last few years, a new platform, lithium niobate on insulator (LNOI), was introduced and has subsequently attracted significant attention.<sup>77,78</sup> Similar to SOI, LNOI relies on smart-cut technology and heterogeneous wafer bonding to transfer submicrometer thick LN films from their native substrate onto  $\text{SiO}_2$  buffer layers, thereby resulting in high index contrast for waveguides to harness the attractive EO properties of LN. Such wafers now are commercially available and have evolved into a promising platform for integrated photonics research.

LNOI has several advantages for quantum applications. The wide bandgap provides a broad transparency window from 310 nm to 4.5  $\mu\text{m}$ . Recent advances in thin film processing and nanofabrication methods<sup>79</sup> have brought the waveguide loss down to a few dB/m at both telecom and visible wavelengths,<sup>81,82</sup> which enables microcavities

**TABLE I.** Comparison between nonlinear materials for chip-scale quantum light generation.

Materials	$\chi^{(2)}$ (pm/V)	$\chi^{(3)}$ (cm <sup>2</sup> /W)	Quality factor, Q	Refractive index @ 1550 nm	Bandgap (nm)	Integration with active devices	References
Si <sub>3</sub> N <sub>4</sub>	...	$2.5 \times 10^{-15}$	$3.5 \times 10^7$ (loaded)	~2	238	No	71
LiNbO <sub>3</sub>	26	$5.3 \times 10^{-15}$	$10^7$ (loaded)	~2.14	310	No	80
GaAs/AlGaAs	180	$2.6 \times 10^{-13}$	$3.52 \times 10^6$ (intrinsic)	~3.4	570–873	Direct	99
SiO <sub>2</sub>	...	$2.2 \times 10^{-16}$	$2.05 \times 10^7$ (intrinsic)	~1.44	137	No	103
Ta <sub>2</sub> O <sub>5</sub>	...	$6.2 \times 10^{-15}$	$3.2 \times 10^6$ (intrinsic)	~2	320	No	104
AlN	1	$2.3 \times 10^{-15}$	$2.5 \times 10^6$ (intrinsic)	~2	205	No	105
SiC	12	$1 \times 10^{-14}$	$1.1 \times 10^6$ (intrinsic)	~2.7	383	No	106
Si	...	$6.5 \times 10^{-14}$	$2.2 \times 10^7$ (intrinsic)	~3.4	1100	Indirect	107
InP	263	$1.1 \times 10^{-13}$	$4.5 \times 10^4$ (intrinsic)	~3.2	922	Direct	108

with a quality factor greater than  $Q = 10^6$ . LN has a relatively large Kerr nonlinearity for SFWM, which has been leveraged for generating Kerr combs.<sup>82,83</sup> The large second-order nonlinear coefficient, which distinguishes LN from the CMOS compatible materials, enables efficient SPDC by using periodically poled lithium niobate (PPLN) waveguides.<sup>52</sup> The cavity-based structure can further boost the efficiency of second order nonlinear processes<sup>84</sup> and finds applications for efficient spectral translation.

The high-speed EO effect in LN is a distinguishing feature from the aforementioned materials for quantum applications. It is significantly faster and efficient compared to thermal phase tuning.<sup>78</sup> The large EO effect also enables microwave photon frequency conversion into the optical domain for quantum state transduction;<sup>85</sup> however, it needs to be pointed out that the EO effect of LN, while larger than other commonly used photonics materials, is still relatively weak when applied in the above-mentioned technologies. For example, for a modulator with  $\pi$ -voltage comparable to standard SOI modulators, centimeter-scale LN waveguides are necessary,<sup>78</sup> which may hinder scalability. Moreover, some other nonlinear effects in this platform, such as the Raman or photorefractive effect,<sup>86</sup> may be deleterious to the performance of many quantum processes. The cost of the LNOI wafer is expensive compared to that of CMOS compatible wafers and, therefore, makes the fabrication process difficult to scale up for high volume production.

#### 4. III-V semiconductors

III-V semiconductors (such as InP, InAs, Al<sub>x</sub>Ga<sub>1-x</sub>As, GaN, AlN, and InSb) are distinguished from all other photonic materials by their high  $\chi^{(2)}$  and  $\chi^{(3)}$  nonlinearities. One of the most attractive properties of these materials for both classical and quantum photonics is the direct bandgap for generating light spanning visible to telecommunication wavelengths. This property makes III-V's widely used for electrically driven lasers that have been heterogeneously grown and integrated with silicon photonics.<sup>87–90</sup> GaAs is a natural host for self-assembled InAs QDs formed through lattice-mismatch-induced strain. The recombination between optically excited electrons and holes confined in the QDs produces a steady stream of ultra-pure single photons on demand, which have found applications for fundamental quantum optics experiments and applications for quantum key distribution, Boson sampling, and information processing. Such capability, along

with both active and passive circuits and waveguide-integrated superconducting nanowire single-photon detectors (SNSPDs),<sup>91</sup> holds the promise for all-on-chip QPICs.

Historically, III-V materials suffer from weak optical confinement and high waveguide propagation loss that have prevented the scaling of pure III-V circuits and their nonlinear applications. To circumvent these issues, III-V-on-insulator photonics was developed in which the III-V layer is placed on a low index dielectric insulator, usually SiO<sub>2</sub>, to form high index contrast for waveguiding. A considerable amount of early effort along this direction was made on AlN<sup>92</sup> and GaN<sup>93</sup> for nonlinear photonics and, more recently, for quantum photonics.<sup>94</sup> Shortly after that, highly nonlinear materials, such as (Al)GaAs<sup>53,95,96</sup> and GaP,<sup>97</sup> were developed. Particularly, the unique combination of high index contrast, large nonlinearities, and a moderate optical bandgap preventing TPA in many cases makes AlGaAs-on-insulator (AlGaAsOI) especially appealing for nonlinear quantum photonics.

A key turning point for AlGaAsOI is the significant reduction of waveguide loss demonstrated in 2020.<sup>98</sup> Notably, for III-V-based waveguides, loss below 0.2 dB/cm has been attained near 1550 nm, with anomalous group velocity dispersion required for frequency comb generation.<sup>99</sup> AlGaAsOI resonators have exhibited Q greater than  $3.5 \times 10^6$ , which is larger than that of SOI and LNOI materials with the same geometry. These improvements were made possible with new photolithography procedures that produced ultra-smooth waveguide profiles, as well as a reduction in the number of crystalline defects, leading to a record low frequency comb threshold. As described in Sec. II C, high nonlinearity, low optical loss, and high-Q microring resonators may lead to a large improvement in the pair generation rate compared to other material platforms. Moreover, these capabilities will also lead to a reduction in the required pump power, relaxing the requirements for on-chip spectral filtering and demultiplexing.

Currently, one limitation for the III-V-on-insulator platform is the relatively high propagation loss at short wavelengths, particularly below 1  $\mu$ m, which is mainly associated with surface defects.<sup>53</sup> A better passivation process can potentially eliminate this loss mechanism to further extend the application range of this platform.<sup>100</sup> Particularly, wide bandgap III-V materials, such as AlN, have enabled resonators with relatively high Q from telecommunication to ultra-violet wavelengths, demonstrating the potential for extending quantum photonic

circuits to short wavelengths.<sup>101</sup> Another challenge for these platforms, compared to Si or SiN platforms, is the lack of well-developed components, which currently is limiting system-level demonstrations. More investigations need to be done along this direction to further exploit this platform; however, considering the fact that the (Al)GaAs fabrication process has been widely used in the current photonics industry, as well as the recent breakthroughs in its direct growth on silicon substrate wafers,<sup>102</sup> AlGaAsOI is capable of relatively inexpensive and high-volume production with potential cost advantages over other novel nonlinear platforms, such as LNOI.

## B. Heralded single-photon generation

Heralded single photons are an important resource for quantum information applications as well as fundamental quantum optical experiments.<sup>103,110</sup> In conventional implementations, pairwise photon generation from SPDC or SFWM produces photons in two optical modes: the heralding mode in which detection of a photon indicates the presence of a single photon in the output mode. Events in which no heralding photon is detected are discarded, which effectively are a post-selection process conditioned on the presence of a photon in the output mode. Ideally, the presence of a photon in the heralding mode would guarantee a single photon in the output mode, but this is not necessarily the case due to optical losses in the experimental setup and detector inefficiency. As a result, the output mode is not in the ideal single-photon state, but rather a mixed state  $\rho_{OM} = p_v|0\rangle\langle 0| + p_1|1\rangle\langle 1|$ , where  $p_v$  ( $p_1$ ) is the probability of the outmode mode to have zero (one) photons conditioned on detection of the heralding

photon. Conceptually, the presence of the vacuum state eliminates the reasoning for heralding in the first place since if  $p_v/p_1 \sim 1$ , this is analogous to unheralded probabilistic single-photon generation.

A schematic of an experimental setup for characterizing heralded single-photon sources is shown in Fig. 4(a). As an example, signal and idler photons are generated using a  $\chi^{(2)}$  microring resonator, the pump is removed with long wavelength (LWP) pass optical filters, and the signal and idler photons are separated through dense wavelength division multiplexing (DWDM). The signal photon is used as the heralding mode, and the idler photon is analyzed using a Hanbury Brown and Twiss interferometer. A histogram of threefold coincidence counts is then recorded to analyze the intensity correlation statistics using a time-correlated single-photon counting (TCSPC) module. An example of the efficiency ( $\eta$ ), count rate, and purity  $[1 - g^{(2)}(0)]$  for a chip-scale heralded single-photon source is shown in Fig. 4(b) for a silica waveguide. With increasing pump power, the count rate increases up to  $\sim 10^5$  counts/s at the expense of the purity due to higher multiphoton generation probability; however, the heralding efficiency is relatively flat at  $\sim 40\%$  across the range of pump powers used in this experiment.<sup>8</sup> Scaling of heralded single-photon sources has also improved in recent years, with examples of 18 SFWM-based silica waveguide sources (four SFWM-resonator sources in silicon) producing single photons with 52% (50%) heralding efficiency, 97% (95%) purity, and 95% (91%) indistinguishability between separate sources.<sup>46,111</sup>

To make an intuitive connection between the heralding efficiency, purity, and count rate, let us consider photon pairs produced from a  $\chi^{(3)}$  microring resonator following the theoretical model in

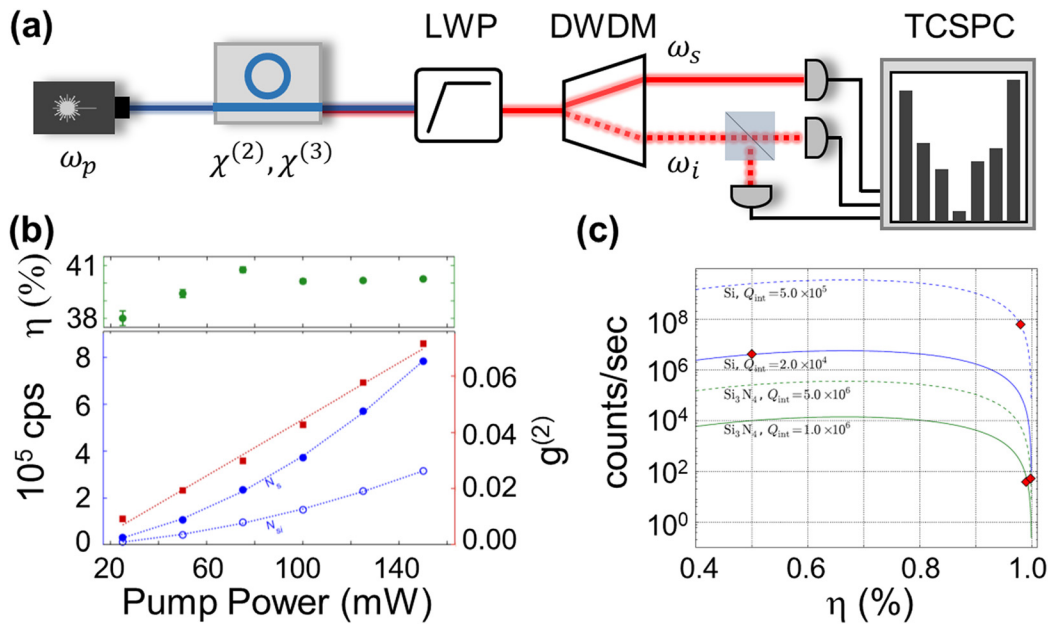


**Fig. 4.** (a) Experimental schematic of heralded single-photon source and Hanbury Brown and Twiss interferometry for measuring heralded second-order intensity autocorrelations. (b) Silica chip-scale heralded single-photon source demonstrating a heralding efficiency of  $\sim 40\%$  and a single-photon purity better than  $\sim 95\%$  (Ref. 8). (c) Theoretical trade-off between source brightness (counts/second) and heralding efficiency ( $\eta$ ). Brightness increases with increasing microring resonator  $Q$  and material nonlinear coefficient (Ref. 112). LWP: long-wave pass filter; DWDM: dense wavelength division multiplexer; TCSPC: time-correlated single-photon counter;  $\omega_p$  = pump frequency;  $\omega_s$  = signal frequency; and  $\omega_i$  = idler frequency. Panel (b) is reproduced with permission from Spring *et al.*, Opt. Express **21**, 13522 (2013). Copyright 2013 The Optical Society. Panel (c) is reproduced with permission from Vernon *et al.*, Opt. Lett. **41**, 788 (2016). Copyright 2016 The Optical Society.

Ref. 112. Assuming we have a pump bandwidth equal to the cavity linewidth so that the signal and idler modes are separable (Schmidt number  $K=1$ ), then the purity of the heralded single-photon source scales as  $(\Gamma^2 + M^2)/(\Gamma + M)^2$ , where  $\Gamma$  is the resonator-waveguide coupling rate and  $M$  is the scattering loss rate. A typical choice for experiments is to design the microring resonator such that  $\Gamma = M$ , i.e., critical coupling. This regime is the ideal design choice if the primary goal is to optimize the output mode flux since the intra-cavity pump photon flux is maximized for a given pump power. Another important metric is the heralding efficiency, which scales as  $\eta = \Gamma/(\Gamma + M)$ . One can then express the heralding rate in terms of the efficiency as  $R_h = \beta \frac{\eta^4(1-\eta)^2}{M^2}$ , where  $\beta$  is a constant related to the third-order optical response and the pump parameters. Counter-intuitively, as the heralding efficiency approaches unity, the heralding rate approaches zero. This is a direct result of the fact that the heralding efficiency is maximum when  $\Gamma \gg M$ , but in this strongly over-coupled regime, the photon flux of the heralding mode is minimized, leading to a suppression of the heralding rate despite unity efficiency. As shown in Fig. 4(c), the heralding rate increases with increasing the  $Q$  and  $\chi^{(3)}$  nonlinear coefficient, as expected. While the scattering rate  $M$  is challenging to control, the coupling rate  $\Gamma$  can be designed to yield either high  $\eta$  or high  $R_h$  depending on the application in mind. Interestingly, optimization of  $\eta$ ,  $R_h$ , and the purity requires operating in the slightly over-coupled regime.

Recent advances in silicon heralded single photon sources have achieved high spectral purity via pump or mode engineering. The modes of the pump, signal, and idler photons can be modified such that the pump resonance quality factor is much smaller than those of the signal and idler, resulting in truly uncorrelated biphoton wavefunctions.<sup>113,114</sup> High spectral purity can also be obtained by utilizing a dual-pump configuration, allowing for the tuning of the temporal response of the resonator.<sup>62,115</sup>

It is worth comparing heralded SPDC and SFWM single-photon sources with other well-studied platforms. Table II shows several important metrics for a variety of quantum emitters in comparison to chip-scale nonlinear sources. A key takeaway is that while arsenide-based QDs are now state-of-the-art for on-demand single-photon generation, nonlinear sources can produce high-quality photons with appreciable brightness and similar single-photon purity, with the advantages of intrinsic scalability and room temperature operation.

### C. Entangled-pair generation

Quantum information can be encoded in photons using several different quantum degrees of freedom, and entanglement on chip has been demonstrated in various forms, including spatial path, frequency-bin,<sup>142</sup> time-bin,<sup>143</sup> polarization,<sup>9,144</sup> and transverse mode.<sup>145</sup> While each form of entanglement has advantages and disadvantages, here we focus the discussion on polarization and time-bin entanglement (see Ref. 146 and Refs. 142 and 147 for a thorough discussion of spatial path and frequency-bin encoding, respectively). Figures 5(a) and 5(b) show methods for producing polarization and time-bin entangled photon pairs through SPDC or SFWM in waveguides (a similar discussion holds conceptually for microresonators).

For polarization entanglement using a type-I  $\chi^{(2)}$  nonlinear medium, a pump photon creates signal and idler photons with the same optical polarization orientation. By designing the photonic waveguide to host both transverse electric and transverse magnetic modes, a 45° polarized pump will produce the bi-photon state  $|\psi\rangle = 1/\sqrt{2} [ |HH\rangle + e^{i\Delta\phi} |VV\rangle ]$ , provided that the probability of four-photon states is significantly smaller than that for two-photon states. The bottom panel of Fig. 5(a) shows an experimental setup for analyzing the bi-photon state. Cross-correlations between the signal and idler photons are recorded using TCSPC for several permutations

**TABLE II.** Comparison between chip-scale single-photon sources (also see Refs. 116–118).

Single-photon system	Brightness (cps)	Lifetime (ns)	Linewidth	Single-photon purity	Indist. (IP)/entangled (EP)	Temp.	References
Arsenide QDs	$\sim 10^7$	$\sim 1$	Lifetime-limited	>99%	IP, EP	4 K	119–122
Nitride QDs	$10^6$	$\sim 0.3$	1.5 meV	>80%	No	RT	123–125
Carbon nanotubes (CNTs)	120 kHz	$\sim 0.1\text{--}0.6$		>99%	No	RT	126,127
Defects in 2D materials (2DMs)	hBN: 4 MHz WSe <sub>2</sub> : 6–37 kHz MoSe <sub>2</sub> : 0.6 kHz	$\sim 1\text{--}5$	N/A	>85%	No	RT 4 K 4 K 4 K	128,129 130,131 132
Color centers in diamond	NV: 1 MHz SiV: 3 MHz	NV: $\sim 10\text{--}20$ SiV: $\sim 1$	Lifetime-limited	$\sim 65\%$ >90%	NV: IP, EP SiV: IP	RT	120,133 120,134
Defects in SiC, ZnO, and rare earths	SiC: 2 MHz ZnO: 100 kHz YAG: 60 kHz	$\sim 1\text{--}4$	N/A	>75%	No	RT	135 136 137
Chip-scale SPDC/SFWM	InP: 145 MHz mW <sup>-2</sup> Si: 149 MHz/mW <sup>2</sup> Si <sub>3</sub> N <sub>4</sub> : 4 MHz mW <sup>-2</sup> LiNbO <sub>3</sub> : 13 MHz/mW	N/A	4–8 GHz 2.1 GHz 30–150 MHz 7–13 MHz	>99% (Heralded)	IP, EP	RT	108 138,139 140 141

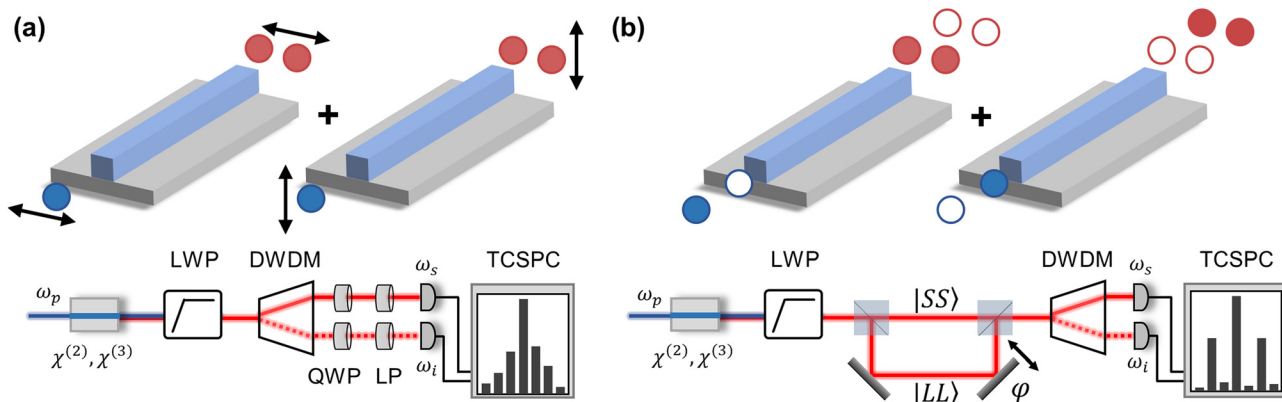


**Fig. 5.** Conceptual illustrations of linear photonic waveguides for the generation of (a) polarization-entangled and (b) time-energy entangled photon pairs. In each case, one (two) pump photon is converted into correlated signal and idler photons for  $\chi^{(2)}$  SPDC [ $\chi^{(3)}$  SFWM] processes. For polarization-entangled photons (a, bottom), recording signal/idler coincidence counts for various polarization bases enables reconstruction of the bi-photon wavefunction and determination of the entanglement fidelity. For time-energy entanglement (b, bottom), the visibility of the interference between coincidence counts between signal/idler photons traveling through the short and long paths of a Franson interferometer vs the relative phase  $\varphi$  provides a measurement of time-bin entanglement. QWP: quarter-wave plate; LP: linear polarizer.

of the detection polarization by rotating a quarter-wave plate (QWP) and linear polarizer (LP) placed before the single-photon detectors. Various criteria for quantifying entanglement exist, with the most stringent being a violation measurement of Bell's inequality using the Clauser–Horne–Shimony–Holt (CHSH) measurement, the fidelity to the anticipated Bell state, and full reconstruction of the photonic quantum wavefunction through quantum state tomography. Each of these cases requires cross-correlation measurements for several nonorthogonal polarizations under the same experimental conditions.<sup>148</sup>

One drawback of polarization entanglement is its susceptibility to depolarization and mixing when propagating long distances through optical fiber or free space due to thermal fluctuations and turbulence. Another kind of bi-photon correlation is time-energy entanglement, which is arguably the most well-suited form of entanglement for communications, as it can be generated and manipulated in QPICs and preserved over long propagation distances in free space or fiber.<sup>149,150</sup> Time-energy entanglement can also enable a higher key generation rate in quantum key distribution.<sup>151</sup> Time-energy entangled pairs can be produced using nonlinear microring resonators with continuous-wave pumping: photon pairs are emitted simultaneously, but their emission time is uncertain within the coherence time of the pump laser, which is typically microseconds or longer [Fig. 5(b)]. This lack of information results in the pairs being time-energy entangled, as originally pointed out by Franson.<sup>152</sup>

Time-energy entanglement can be quantified by measuring violations of Bell's inequalities using a Franson interferometer for time-bin encoding, shown in the bottom panel of Fig. 5(b). Signal and idler photons generated by a continuous wave pump are sent into a folded Mach–Zehnder interferometer, followed by DWDM and single-photon detection. The generated histograms from signal-idler cross correlation measurements will feature a central peak with two adjacent delayed peaks. These correspond to coincidence detection events for when both the signal and idler travel through the short ( $|SS\rangle$ ) or the long ( $|LL\rangle$ ) interferometer path, the signal through the short path and idler through the long path ( $|SL\rangle$ ), and vice versa ( $|LS\rangle$ ), respectively. Post-selection on the central signal-idler zero-delay peak produces a time-bin entangled state  $|\psi\rangle = 1/\sqrt{2} [|SS\rangle + e^{i\Delta\varphi} |LL\rangle]$  since

information regarding which path the photons took is not known. Analogous measurements in the frequency domain are possible using fast phase-modulation techniques.<sup>147</sup>

Results from on-chip time-bin entanglement from a silicon microring resonator are shown in Fig. 6.<sup>143</sup> The transmission spectrum shows a series of resonances separated by the cavity free spectral range. The pump laser is tuned in to resonance with the  $\sim 1550$  nm peak, and signal and idler photons are produced at adjacent peaks via SFWM. The internal and off-chip single generation rates are shown in Fig. 6(b), with a possible onset of TPA at the highest pump powers. The first step for verifying entanglement is to demonstrate that the signal and idler photons are produced in pairs. Figure 6(c) shows a coincidence measurement using a Franson-type interferometer with one of the arms blocked, verifying simultaneous pair generation. By unblocking both arms, the coincidence histogram shown in Fig. 6(d) features two adjacent peaks in addition to the central peak, as expected and previously described for time-bin entanglement. By sweeping the phase of one of the arms, the visibility of the central peak interference pattern provides quantitative proof for violation of Bell's inequality.

Similar experiments have been performed in a variety of photonic material platforms, including InP shown in Fig. 6(f). The internal generation rates for SFWM are comparable to the silicon platform, which scale approximately as<sup>108</sup>

$$R_g = (\gamma 2\pi R)^2 \left( \frac{Qv_g}{\pi\omega_p R} \right)^3 \frac{v_g}{4\pi R} P_p^2, \quad (2)$$

where  $\gamma$  is the nonlinear coefficient,  $R$  is the microring resonator radius,  $Q$  is the quality factor,  $v_g$  is the group velocity at the pump wavelength,  $\omega_p$  is the pump angular frequency, and  $P_p$  is the on-chip pump power. Equation (2) demonstrates that the internal generation rate scales as  $\gamma^2 Q^3 R^{-2} P_p^2$ ; thus, microring resonators with higher material nonlinearity, smaller radius, and higher quality factor will produce entangled photons at a higher rate for a given pump power. The on-chip pair generation rate is given by  $PGR = R_c / (\eta_i \eta_s)$ ,<sup>11</sup> where  $\eta_s$  ( $\eta_i$ ) is the collection and detection efficiency of the signal (idler) photons and  $R_c$  is the detected coincidence rate. This expression can also be written as

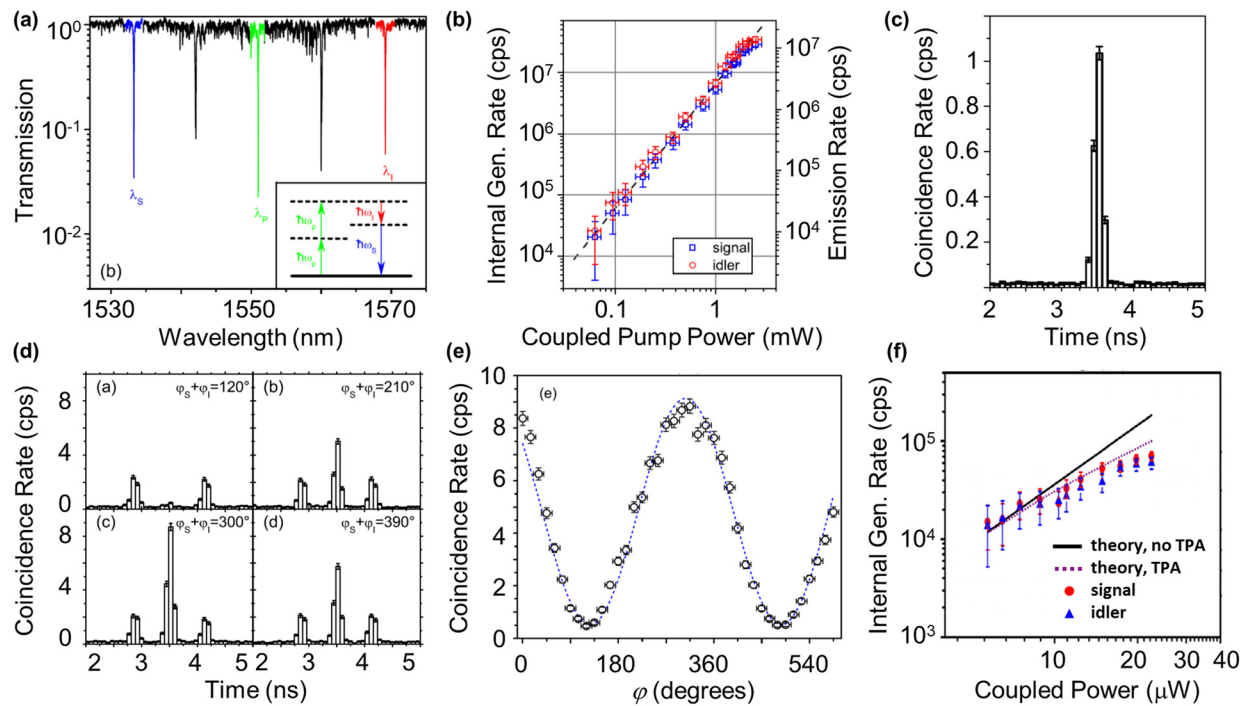


**Fig. 6.** (a) The transmission spectrum of a silicon on silica microresonator. A continuous-wave pump laser tuned to the central 1550 nm resonance generates signal and idler photons at adjacent sidebands through SFWM (inset). (b) Signal and idler internal generation rate (left) and emission rate (right) vs coupled on-chip pump power. (c) Coincidence count rate histogram for 1 mW coupled pump power. (d) Coincidence histogram measured at the output of a Franson-type interferometer for a 1.5 mW coupled pump power over an integration time of 120 s. The three peaks correspond to coincidences between signal and idler photons traveling through the long/short, short/short or long/long, and short/long paths of the interferometers, respectively. (e) Coincidence counts of the central peak in (d) vs interferometer relative phase  $\varphi$ . The visibility of the oscillations in the two-photon interference between the short/short and long/long paths provides a measure of the degree of entanglement. (f) Signal and idler generation rate for an InP microring resonator demonstrating two-photon absorption, which limits the maximum generation rate for InP- and silicon-based sources. Data shown in (a)–(e) were adapted with permission from Grassani *et al.*, Optica **2**, 88 (2015). Copyright 2015 Authors, licensed under the terms of the OSA Open Access, and data in (f) were adapted with permission from Kumar *et al.*, Appl. Phys. Lett. **114**, 021104 (2019). Copyright 2019 AIP Publishing.

$PGR = R_i R_s / R_c$ , where  $R_s$  ( $R_i$ ) is the signal (idler) detected count rate. In addition to the generation rates, the signal-to-noise ratio (SNR) is a key metric for entangled-pair source applications. The SNR is determined by measuring the coincidence-to-accidental ratio (CAR) by dividing the integrated area of the central histogram peak by the average of the background counts. Typical values for these parameters are shown in Table III for different materials. An interesting comparison between Si and InP microring resonators is shown in the top two rows. Both platforms achieve similar PGR through cavity-enhanced SFWM, but in different ways. The Si resonators exhibit larger  $Q$ , but the  $\chi^{(3)}$  nonlinearity is higher in InP. While these are some of the highest PGR values reported to date, it is worth noting that the AlGaAsOI platform exhibits larger nonlinearity and  $Q$  values than both these specific demonstrations.<sup>98</sup> It is important to note that the brightness of the source can be defined as the PGR normalized to the optical bandwidth of the signal or idler modes. Typically, high- $Q$  microresonator geometries are the brightness sources because photon pairs are emitted into ultra-narrow spectral modes compared to nonresonant devices.

#### D. Squeezed light

The Heisenberg uncertainty principle places a lower bound on the measurement imprecision of the photon number and phase.

The minimum level of noise in an optical measurement that can be attained without the use of squeezed light—the standard quantum limit (SQL)—is due to the shot noise of the laser. Squeezed states of light provide a way to reduce, or squeeze, the noise in one of the two field quadratures below the SQL, shown in Fig. 7(a) for phase-squeezed light, with a concomitant antisqueezing in the other quadrature. Squeezed states of light are an important resource for precision measurements and have been utilized for improved signal-to-noise in sensors,<sup>154</sup> metrology,<sup>155,156</sup> spectroscopy,<sup>157</sup> and continuous-variable (CV) quantum information processing.<sup>158</sup>

Several pioneering techniques were developed in the mid-1980s for generating squeezed states optically, most notably through degenerate four-wave mixing (DFWM) with atomic ensembles,<sup>159</sup> self-phase modulation in  $\chi^{(2)}$  materials, and DFWM in  $\chi^{(3)}$  materials. For the last three decades, the workhorse for generating squeezed-light has been an optical parametric oscillator (OPO) cavity, where a  $\chi^{(2)}$  or  $\chi^{(3)}$  nonlinear crystal is placed in the cavity that can be operated either below or above threshold. Both SPDC and SFWM can produce two-mode squeezed states, where cross-correlations of the signal and idler, created in separate spatial or spectral modes, exhibit squeezing. Single-mode squeezed states can be produced by DFWM, where the signal and idler are created in the same mode with  $\omega_s = \omega_i$ . The amount of

**TABLE III.** Comparison between chip-scale time-energy entangled-pair sources.

Entangled-pair system	Quality factor Q	Pair generation rate	Visibility	CAR	Single-photon purity	References
Si	$\sim 10^5$	$149 \text{ MHz mW}^{-2}$	98%	532	90%	139
InP	$4 \times 10^4$	$145 \text{ MHz mW}^{-2}$	78%	277	...	108
LiNbO <sub>3</sub>	...	$23 \text{ MHz mW}^{-1}$	N/A	668	82%	52
AlN	$\sim 10^5$	$6 \text{ MHz mW}^{-1}$	...	560	91%	94
Si <sub>3</sub> N <sub>4</sub>	$2 \times 10^6$	$4 \text{ MHz mW}^{-2}$	90%	$\sim 10$	...	140
(Al)GaAs	...	$2 \text{ MHz mW}^{-1}$	...	113	...	153

squeezing is proportional to the ratio of the coupling out of the cavity to the total loss ( $\eta_c$ ) through the expression  $S(\Omega) = 1 - \eta_c \eta_d / (1 + \Omega^2 \tau_c^2)$ , where  $\eta_d$  takes into account loss from the source to the detector and the detector efficiency,  $\Omega$  is the sideband measurement frequency, and  $\tau_c$  is the cavity photon lifetime proportional to the quality factor Q. It is evident that loss is deleterious to squeezing, and improving the cavity quality factor can improve squeezing. Below threshold, the amount of squeezing can be tuned by adjusting the pump power, but above threshold, the amount of squeezing is clamped. Alternatively, the squeezed state can be tuned externally to the OPO by introducing loss at the expense of reduced photon flux, and this requires large pump powers to generate the initial squeezed state.

Integrated photonics provides a more nascent approach to generating squeezed light in a compact, monolithic chip with a small footprint and low consumption power. For many applications, such as quantum key distribution with CV-entangled photons, a large squeezing bandwidth is desirable for achieving high-speed communication. Generally, there is a trade-off between the amount of squeezing and the bandwidth. On the one hand, a high-finesse cavity improves the squeezing. On the other hand, high finesse typically leads to a reduced bandwidth. Several microring resonator platforms have been

developed to simultaneously optimize both the squeezing and the bandwidth, which are summarized in Table IV. These are based on lithium niobate,<sup>160</sup> silicon,<sup>161</sup> and silicon nitride,<sup>162,163</sup> with  $-5 \text{ dB}$  of squeezing possible when correcting for losses across a GHz bandwidth. Notably, similarly large squeezing can be achieved with PPLN waveguides without the fundamental bandwidth trade-off of cavity geometries.<sup>164</sup> Table IV contrasts the chip-scale squeezing platforms with table-top optical parametric cavities, which remain state-of-the-art with  $15 \text{ dB}$  of squeezing made available for precision metrology, for example, gravitational wave observatories.<sup>165</sup>

One example of a chip-scale squeezed source is shown in Fig. 7(b).<sup>166</sup> Two pump lasers are coupled onto a silicon nitride chip and split using multimode interferometers into two separate microring resonators, where signal and idler photons are produced in each via DFWM. One resonator is pumped above threshold and serves as the local oscillator for homodyne detection. The other resonator is pumped below threshold to generate the squeezed mode. The noise power out of the homodyne detector is analyzed using a radio-frequency spectrum analyzer (RFSA) and quantitatively compared with the shot noise of the local oscillator to determine the frequency spectrum of the squeezing as the relative phase between the local

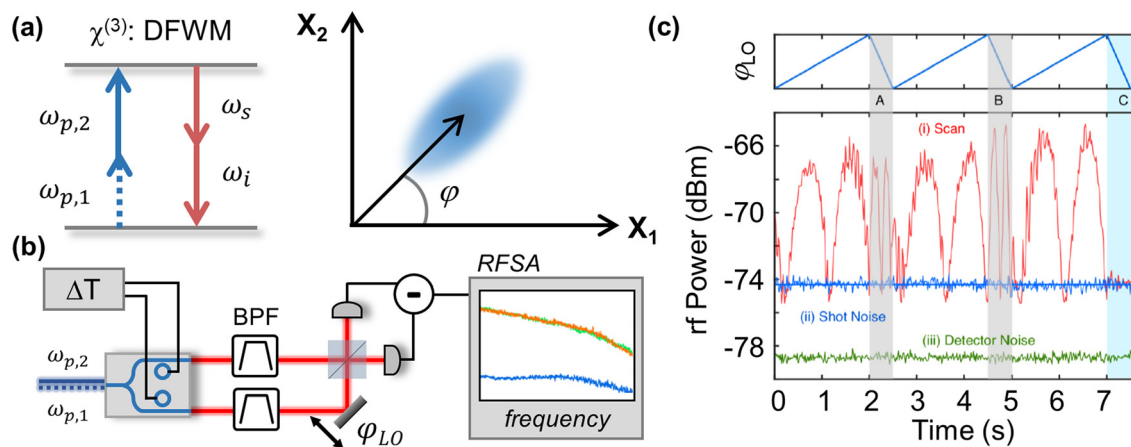


**Fig. 7.** (a) Degenerate FWM (DFWM) for single-mode squeezing, where two nondegenerate pump photons of frequencies  $\omega_{p,1}$  and  $\omega_{p,2}$  are converted into degenerate signal and idler photons at frequency  $\omega_s = \omega_i$ . An illustration of the single-mode squeezed state is shown on the right, showing that phase squeezing leads to larger fluctuations in the amplitude uncertainty. (b) Schematic of a homodyne experimental setup for measuring squeezing. Pump lasers are coupled onto the chip and split with a multimode interferometer into two ring microresonators, where they produce signal and idler photons via DFWM. One resonator is pumped above oscillation threshold and serves as an intense local oscillator, while the other resonator is pumped below threshold to produce the squeezed mode. Homodyne detection of the noise power using a radio-frequency spectrum analyzer (RFSA) enables careful measurements of the amount of squeezing relative to the local oscillator shot noise, as shown in (c). Data in the figure are reproduced with permission from Zhao *et al.*, Phys. Rev. Lett. **124**, 193601 (2020). Copyright 2020 American Physical Society.

**TABLE IV.** Comparison between chip-scale squeezed-light sources.

Squeezed-light system	Geometry	Nonlinear process	Prop. loss/Q	Squeezing (antisqueezing)	Bandwidth	References
PPLN	Waveguide	$\chi^{(2)}$	4 dB/m (1560 nm) 1 dB/cm (780 nm)	2.00 dB (2.80 dB)	70 nm	<a href="#">167</a>
PPLN	Waveguide	$\chi^{(2)}$	Optical loss: 0.79% W <sup>-1</sup>	6.3 dB (15 dB)	2.5 THz	<a href="#">168</a>
GaAs (AlGaAs) $\text{Si}_3\text{N}_4$	Waveguide Microring	$\chi^{(3)}$ $\chi^{(3)}$	Linear loss coefficient: -6.3 cm <sup>-1</sup> 0.28 dB/cm Propagation loss	4.5 dB (Estimated) 3.09 dB (On chip) (Q = 1.3 × 10 <sup>6</sup> )	... ... 1.5 dB (4.3 dB)	<a href="#">169</a> <a href="#">166</a> <a href="#">170</a>
Si $\text{SiO}_2$	Microring Optical fiber	$\chi^{(3)}$ $\chi^{(2)}$	Q = 0.166 × 10 <sup>6</sup> ...	0.2 dB 3.3 dB (16.8 dB)	10 MHz ... ...	<a href="#">161</a> <a href="#">171,172</a>
Table-top OPO	Crystal-based	$\chi^{(2)}$	Optical loss: 2.5%	15 dB (11 dB)	84 MHz	<a href="#">165,173</a>
ZnS PPKTP	Crystal-based Crystal-based	$\chi^{(3)}$ $\chi^{(2)}$	...	2.2 dB 12.7 dB (19.9 dB)	30–50 MHz ... ...	<a href="#">174</a> <a href="#">175</a>
CdSe	Crystal-based	$\chi^{(3)}$	Optical loss: 4%	0.4 dB	...	<a href="#">176</a>

oscillator and squeezed mode is swept in time [Fig. 7(c)]. In this example, ~1.3 dB of squeezing is possible although significant antisqueezing in the other quadrature suggests that there is significant loss limiting the amount of attainable squeezing in the experiment. Despite the modest amount of squeezing, this is an exemplary result for fully tunable, chip-scale squeezing in a CMOS-compatible process that may pave the way for all-on-chip CV quantum protocols.

### III. QUANTUM FREQUENCY TRANSLATION AND STATE MANIPULATION

At the heart of nonlinear photonics is the creation of new optical frequencies through nonlinear light-matter interactions between a pump field and a  $\chi^{(2)}$  or  $\chi^{(3)}$  medium. Spectral translation of signals, i.e., the ability to convert single and entangled photons across octave-spanning bandwidths from visible to telecommunication wavelengths, will be a key enabling technology for networking disparate quantum information systems and sensors, synchronization and timing for optical clocks, and serving as wavelength references.<sup>177</sup> Figure 8(a) shows the various technologies for spectral translation, ranging from light-matter coupling in a two-level system ( $\sim 10^{-4}$  μm translation) to  $\chi^{(2)}$  periodically poled waveguides ( $\sim 1$  μm translation), with  $\chi^{(3)}$  materials falling in between.<sup>178</sup> Spectral translation of classical signals in various  $\chi^{(2)}$  and  $\chi^{(3)}$  materials and device geometries have been realized, including LiNbO<sub>3</sub>,<sup>179</sup> Si,<sup>180</sup> Si<sub>3</sub>N<sub>4</sub>,<sup>181</sup> GaP,<sup>182</sup> AlN,<sup>183</sup> and (Al)GaAs,<sup>95</sup> which are paving the way for translation of quantum signals. The key figures of merit are the translation efficiency  $\eta_t = P_{\text{SHG}}/P_{\text{PUMP}}$  for SHG ( $\eta_t = P_{\text{translated}}/P_{\text{signal}}$  for other processes) and the quantum efficiency defined as  $\eta_Q = N_{\text{SHG}}/N_{\text{PUMP}}$  for SHG ( $\eta_Q = N_{\text{translated}}/N_{\text{signal}}$  for other processes).

Several important milestones have been achieved in the last few years, which are summarized in Table V. One notable example from 2019 is shown in Fig. 8(b) in which a 1570 input signal is translated to

670 nm by pumping a silicon nitride microring resonator at 970 nm.<sup>73</sup> Lu *et al.* achieved translation over 250 THz with a translation efficiency exceeding 30% using a pump power of only  $\sim 330 \mu\text{W}$ . This corresponds to a translation efficiency of 274% mW<sup>-1</sup>, which is an order of magnitude improvement over previous nanophotonic devices. Another exciting development is the second-harmonic conversion of a 2 μm signal to 1 μm in a heterogeneous GaAs-on-insulator waveguide.<sup>95</sup> A record conversion efficiency of 46% mW<sup>-1</sup> cm<sup>-2</sup> is achieved over a signal bandwidth of 148 GHz by minimizing the propagation loss and optimizing phase matching. Spectral translation of a single photon was also achieved in the same year.<sup>178</sup> Single photons produced on-demand from an InAs QD embedded in a micropillar cavity at 4 K were coupled into a Si<sub>3</sub>N<sub>4</sub> microring cavity. Through FWM Bragg scattering, single photons are shifted by up to ~10 nm with an on-chip efficiency of ~12%, limited by the QD linewidth. Crucially, antibunching of the translated photons is still observed as shown in Fig. 8(c) for both continuous wave and pulsed pump excitation. Improvements in the conversion efficiency are possible by utilizing QDs with narrower transform-limited linewidths at least a few times smaller than the resonator linewidth and exploring other translation device geometries, including the ultra-efficient, high-bandwidth GaAs-on-insulator waveguides.

Related to spectral translation is the on-chip frequency control of single- and entangled-photons, which finds applications for frequency-bin entanglement and programmable tuning of the bi-photon JSI. Figure 9(a) illustrates this concept: a frequency comb generated with a silicon nitride microring resonator is modulated using pulse shapers and radio-frequency phase modulators.<sup>147,184</sup> Imany *et al.* are able to identify up to 40 frequency modes from the JSI, and adjacent modes are superimposed through 50 GHz electro-optic phase modulation to verify entanglement in a frequency domain experiment analogous to temporal Franson interferometry. This demonstration

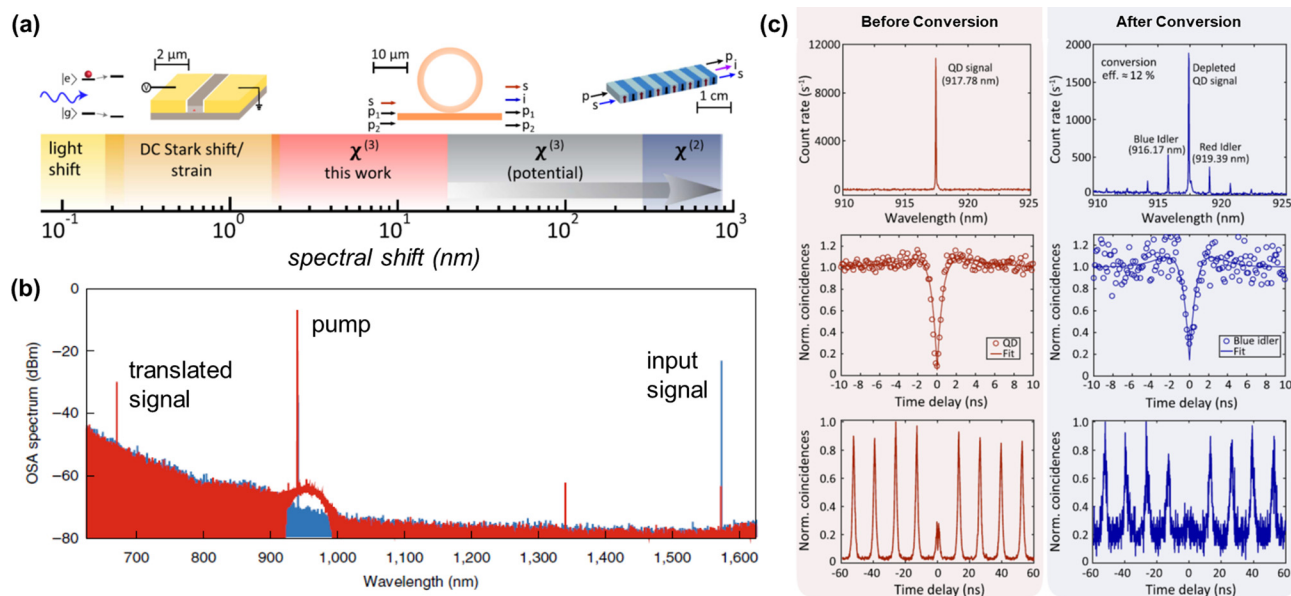


**Fig. 8.** (a) Frequency shift techniques for quantum photonic translation. The largest shifts of up to 100s of nanometers are obtained through  $\chi^{(2)}$  processes in engineered centimeter-long waveguides. (b) Spectral translation from 1570 nm to 670 nm via 970 nm pumping of a  $\chi^{(3)}$  microring resonator (Ref. 73). (c) Single-photon frequency translation of on-demand photons emitted from a self-assembled InAs quantum dot (Ref. 178). Panel (b) is reproduced with permission from Lu *et al.*, Nat. Photonics 13, 593 (2019). Copyright 2019 Springer Nature. Panel (c) is reproduced with permission from Singh *et al.*, Optica 6, 563 (2019). Copyright 2019 Authors, licensed under the terms of the OSA Open Access Publishing Agreement.

provides exciting opportunities for higher-dimensional entanglement for high-capacity quantum computing and communications. Spectral shaping of the JSI is also possible on chip as shown in Fig. 9(b). A series of five coupled silicon microring resonators produces a JSI as

shown in the top-right panel.<sup>55</sup> By tuning the pump wavelength or the chip temperature, off-diagonal slices of the JSI can be accessed, enabling *in situ* control of the photon spectra and the Schmidt number, as shown in the bottom panels.

**TABLE V.** Comparison of frequency-conversion devices.

Material	Geometry	Nonlinear process	Size ( $\mu\text{m}$ ): rings: $r/w/h$ , waveguides: $L/w/h$ , disks: $r/h$ , and spheres: $r$	$\lambda_s - \lambda_t$ (nm)	$\eta$ [ $\chi^{(2)}$ : %/mW] [ $\chi^{(3)}$ : %/mW $^2$ ]	References
$\text{Si}_3\text{N}_4$	Microring	$\chi^{(3)}$ , dFWM	25/1.15/0.5	1570 – 670	274	73
AlN	Microring	$\chi^{(2)}$ , SFG	30/1.12/1	1538 – 774	2.6	185
$\text{LiNbO}_3$	Microring	$\chi^{(2)}$ , SHG	50/0.69/0.55	1550 – 775	1.5	186
GaAs	Microring	$\chi^{(2)}$ , SHG	100/1.3/0.15	2000 – 1000	0.04	187
AlN	Microring	$\chi^{(2)}$ , SHG	30/1.24/1.1	1550 – 775	17	188
$\text{LiNbO}_3$	Microdisk	$\chi^{(2)}$ , SHG	51/0.7	1540 – 770	0.11	189
GaP	Microdisk	$\chi^{(2)}$ , SHG	3.3/0.25	1545 – 772	$4.4 \times 10^{-4}$	182
$\text{SiO}_2$	Microsphere	$\chi^{(2)}$ , SHG	62	1550 – 775	$4.9 \times 10^{-5}$	190
$\text{LiNbO}_3$	mm-Resonator	$\chi^{(2)}$ , SHG	1900/500	1064 – 532	300	191
PPLN	mm-Resonator	$\chi^{(2)}$ , SHG	1500/500	1550 – 775	2.4	192
PPLN	Waveguide	$\chi^{(2)}$ , SHG	4000/1.4/0.6	1500 – 775	0.4	179
GaAs	Waveguide	$\chi^{(2)}$ , SHG	1400/1.53/0.150	2000 – 1000	0.25	53
$\text{Si}_3\text{N}_4$	Waveguide	$\chi^{(2)}$ , SFG	40 000/1.5/0.87	1547 – 773	$3.3 \times 10^{-4}$	193
$\text{Si}_3\text{N}_4$	Waveguide	$\chi^{(3)}$ , dFWM	40 000/1.5/0.87	1547 – 1540	$9.8 \times 10^{-8}$	193
Si	Waveguide	$\chi^{(3)}$ , dFWM	20 000	3550 – 1590	0.18	180
PPGaN	Waveguide	$\chi^{(2)}$ , SHG	1 200 000/.../4	1658.6 – 829.3	0.013	194
GaAsOI	Waveguide	$\chi^{(2)}$ , SHG	2900/1.3/0.149	2000 – 1000	40	95
AlGaAsOI	Waveguide	$\chi^{(2)}$ , SHG	2689/0.74/0.100	1560 – 780	12.02	195

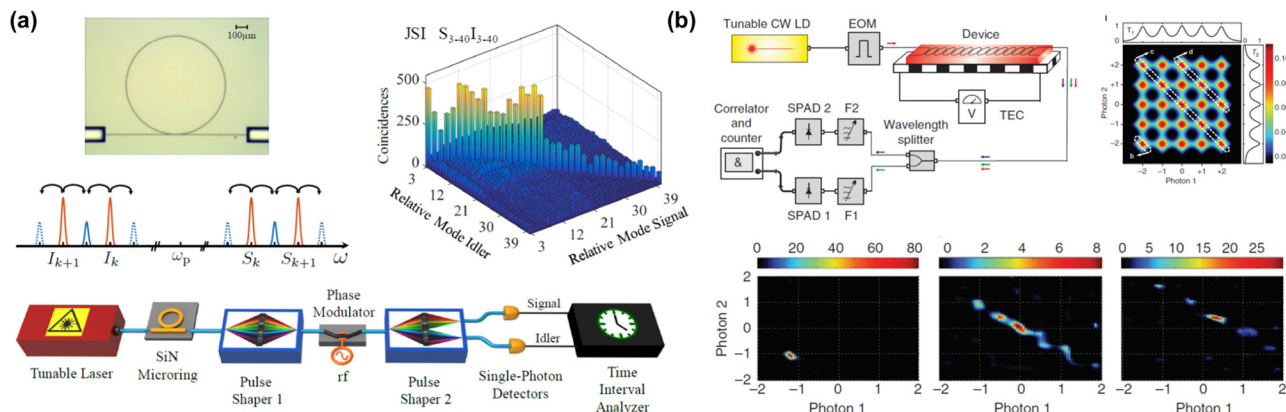


**Fig. 9.** (a) Silicon nitride on a silica microring resonator for correlated pair generation of up to 40 modes adjacent to the pump frequency (Ref. 146). The joint spectral intensity appears as a series of microcomb lines. Frequency-bin entanglement between modes  $S_k$  and  $I_k$  is measured using the pulse shaper and phase modulator setup in the bottom panel. (b) The joint spectral intensity from a silicon microring resonator device with five coupled rings (Ref. 55). By tuning the pump frequency or the chip temperature, off-diagonal slices can be accessed, providing a method for *in situ* control of the photon spectrum and Schmidt number—a widely used metric for entanglement. Panel (a) is reproduced with permission from A. S. Solntsev and A. A. Sukhorukov, Rev. Phys. 2, 19 (2017). Copyright 2017 The Optical Society. Panel (b) is reproduced with permission from Kumar *et al.*, Nat. Commun. 5, 1 (2014). Copyright 2014 Springer Nature Open Access.

#### IV. SYSTEM-LEVEL INTEGRATION AND APPLICATIONS

The applications using quantum light range from quantum computing and communication to sensing and imaging. Here, we present some of the recent demonstrations utilizing chip-scale quantum light sources as well as how these light sources can be integrated with other photonic components to reduce optical loss and improve computing and communication performance.

Emerging quantum photonic technologies will likely leverage the low-loss optical fiber networks and high-speed photonic interconnect technologies developed for optical telecommunications. As such, most research in quantum photonics focuses on 1550 nm sources, modulators, circuits, and detectors that can also take advantage of the scalability and reliability of silicon CMOS foundry processing. An example is shown in Fig. 10(a), where entanglement is distributed between remote silicon photonic chips separated by 10 m of optical fiber.<sup>111</sup> Path-entangled states are created on the first chip using SFWM in spiral waveguides and then transferred to the second chip for analysis and detection. Chip-to-chip coupling also serves the purpose of additional filtering required to remove the optical pump laser. By combining high-speed modulators with integrated laser sources, thermo-optic phase shifters, and delay lines, chip-to-chip quantum key distribution across network-scale distances has been demonstrated,<sup>117</sup> as shown in Fig. 10(b).

While quantum photonics is already making an immediate impact on secure communications and networks, longer-term goals include universal quantum computing and quantum simulations. Different protocols and architectures are shown in Figs. 10(c)–10(f). Silicon photonics is the most mature platform for quantum optical computing, with measurement-based quantum computing using four qubits,<sup>47</sup> quantum teleportation,<sup>196</sup> fully reprogrammable two-qubit operations and multidimensional entanglement,<sup>30</sup> and two-qubit gates based on time-bin encoding<sup>184</sup> demonstrated in the last few years. Figure 11 illustrates the scale of QPIC technologies as of 2018. The number of components integrated onto a single chip shows exponential growth over the last decade, with nearly 10 000 components

expected by 2022. Many of the large-scale quantum photonic circuits have been demonstrated on CMOS-compatible platforms, particularly SOI, as these fabrication processes have been well-studied and allow for the creation of scalable, high-quality photonic chips. Figure 11(b) demonstrates more than 550 components on an individual quantum photonic chip,<sup>29</sup> with current state-of-the-art exceeding 650 components. The chip includes 16 identical spiral waveguide photon-pair sources used to create a highly entangled qubit state by cascaded multiple Mach-Zehnder interferometers. While it still requires off-chip optical pumping and single-photon detectors to complete quantum state tomography and multidimensional Bell correlation measurements, recent advances in waveguide-coupled superconducting nanowire single-photon detectors (SNSPDs)<sup>91,197,198</sup> will enable all-on-chip computing although detector integration will introduce additional challenges with silicon photonics at cryogenic temperatures. Nonetheless, the integration of single photon detectors would improve the detection efficiency by eliminating the output coupling loss (typically a few dB/coupler), allowing for faster computation rates and lower error rates.

#### V. OUTLOOK

Following rapid and sustained research leading to improvements in nanofabrication processing and demonstrations of prototype quantum optical device technologies, the field of integrated quantum photonics has reached a critical point: on one hand, the emergence and sophistication of various photonic material platforms have enabled a large amount of device-level demonstrations for quantum light generation and some preliminary system level applications.<sup>87,95,98,199,200</sup> On the other hand, significant challenges still remain that must be addressed in order to take advantage of the performance and functionality of nonlinear sources with fully integrated, chip-scale quantum photonic circuits.

One challenge is the high optical pump power required to generate photon pairs in nonlinear materials with appreciable flux. Although the efficiency of nonlinear photon sources has seen dramatic

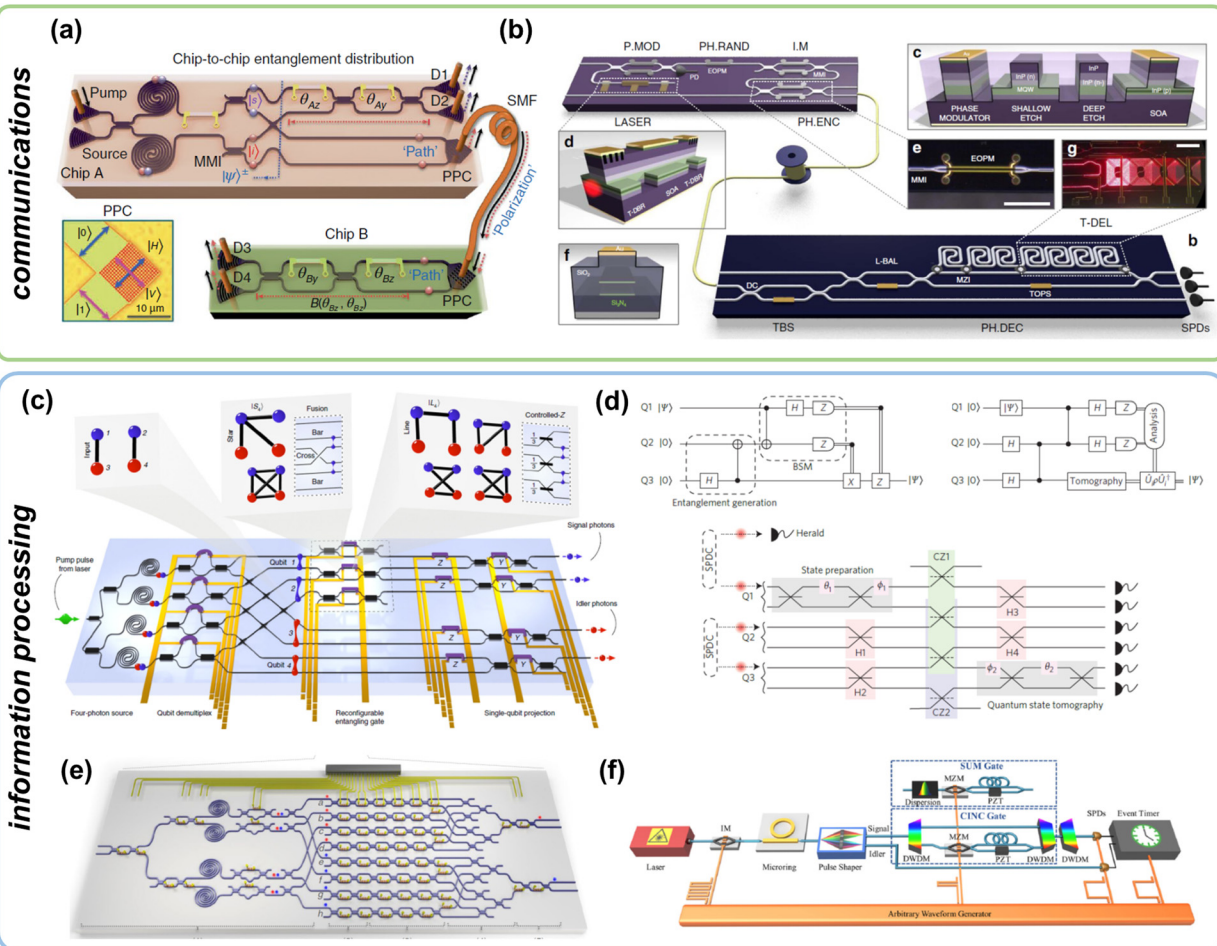


**Fig. 10.** (a) Silicon chip-to-chip entanglement distribution platform linked by a 10 m single-mode optical fiber. Path-entangled states are created on the first  $\sim 1 \times 1 \text{ mm}^2$  chip using SFWM spiral waveguides and then transferred to the second chip (Ref. 42). (b) A chip-to-chip quantum key distribution network (Ref. 17). The transmitter chip comprises a tunable InP laser, electro-optic phase modulators, and interferometers, while the receiver comprises thermo-optic phase shifters and reconfigurable delay lines. (c) Silicon photonic chip for generating, manipulating, and measuring four-photon, four-qubit graph states for measurement-based quantum computing (Ref. 47). (d) A silica chip for quantum teleportation of photonic qubits (Ref. 196). Qubits 2 and 3 are prepared in an entangled state, and a Bell-state measurement is performed on qubits 1 and 2 to teleport the state to qubit 3. (e) A fully reprogrammable silicon quantum photonic chip capable of universal two-qubit quantum information processing (Ref. 30). The chip comprises four SFWM spiral waveguide sources, 58 thermo-optic shifters, and 82 multimode interferometers. (f) Experimental setup for implementing two-qubit gates based on time-bin encoding (Ref. 184). Panel (a) is reproduced with permission from Wang *et al.*, Optica 3, 407 (2016). Copyright 2016 Authors, licensed under the terms of the OSA Open Access. Panels (b) and (c) are reproduced with permission from Sibson *et al.*, Nat. Commun. 8, 13984 (2017). Copyright 2017 Springer Nature Open Access and reproduced with permission from Adcock *et al.*, Nat. Commun. 10, 1 (2019). Copyright 2019 Springer Nature Open Access. Panels (d) and (e) are reproduced with permission from Metcalf *et al.*, Nat. Photonics 8, 770 (2014). Copyright 2014 Springer Nature and reproduced with permission from Qiang *et al.*, Nat. Photonics 12, 534 (2018). Copyright 2018 Springer Nature. Panel (f) is reproduced with permission from Imanry *et al.*, npj Quantum Inf. 5, 59 (2019). Copyright 2019 Springer Nature Open Access.

improvement over the last few years due to advances in microring resonator  $Q$  and waveguide propagation loss, currently, the pair brightness is still lower compared to two-level emitters based on cavity-coupled InAs QDs. As a result, the pump power required in current system-level demonstrations is significantly higher than the generated photon power, placing strict requirements for optical filters to reject the pump. Considering a 1550 nm pump power of  $1 \mu\text{W}$ , for example, more than 130 dB of pump rejection is required to suppress any pump photons from reaching single-photon detectors. On-chip filtering components include ring resonators, Fabry Perot cavities,

Mach-Zehnder interferometers, and Bragg gratings. Cascading them to form multistage structures in theory can achieve arbitrarily high extinction ratios, but in practice, scattered pump light from the substrate or different components in the circuits ultimately limits the filtering performance. As a consequence, in many experiments, two separate chips linked by fibers have to be used to realize sufficient pump suppression. Several steps can be taken to mitigate these issues. The first is to utilize materials with high nonlinear coefficients and microresonators with high  $Q$  and small radii to enhance the generation rate and reduce the required pump power. The second is to

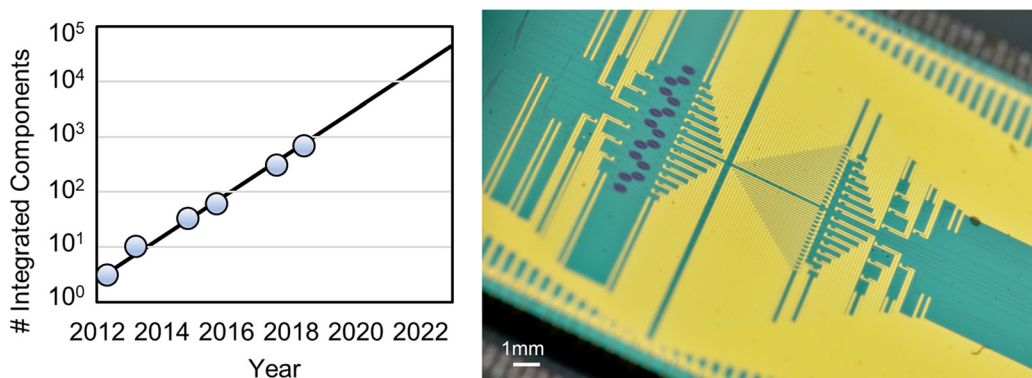


**Fig. 11.** Scaling of the number of integrated components on a single photonic chip for quantum information applications. The chip on the right combines 16 SFWM sources, 93 thermo-optic phase shifters, 122 multimode interferometers, 376 waveguide crossers, and 64 grating output couplers. Adapted with permission from Wang *et al.*, *Science* **360**, 285 (2018). Copyright 2018 The American Association for the Advancement of Science.

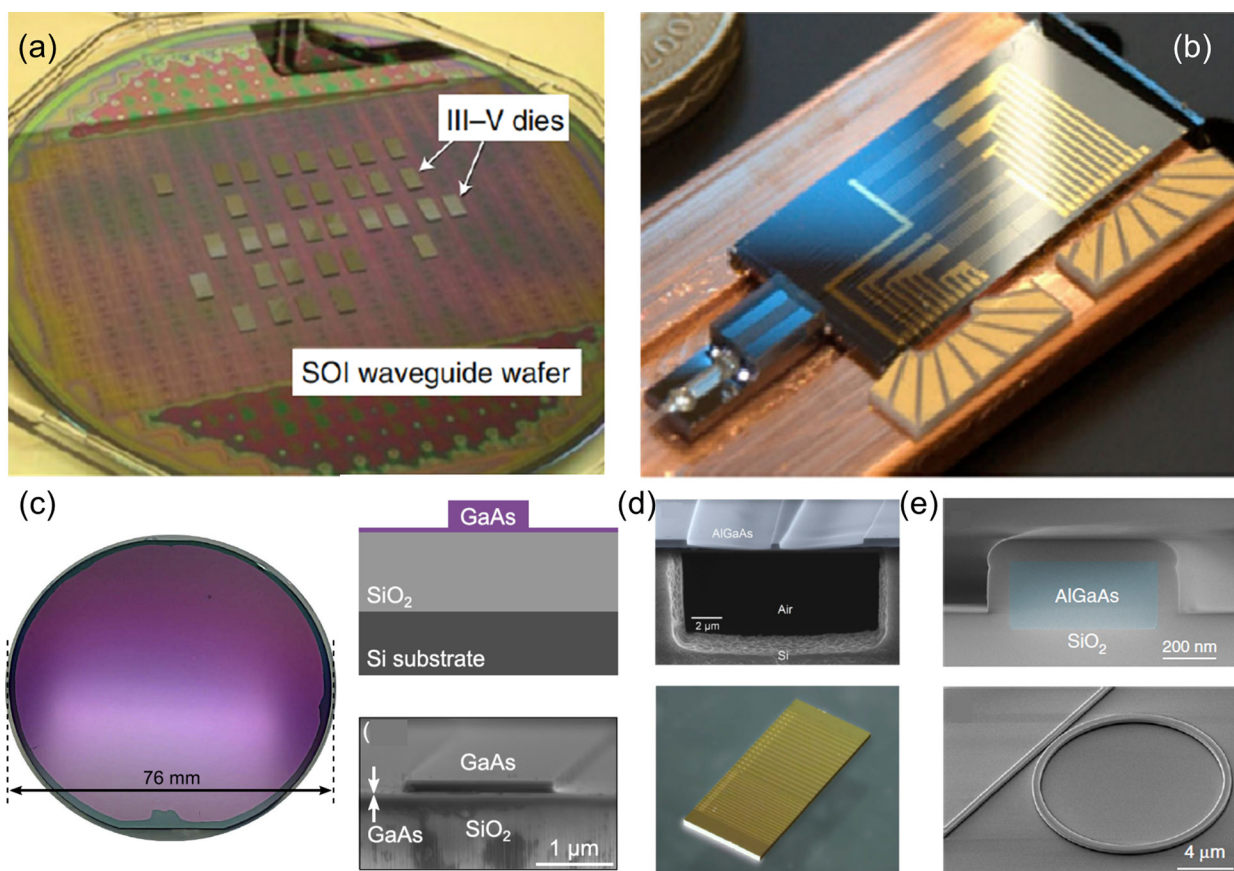


**Fig. 12.** Advances in heterogeneous photonic integration methods are enabling the unification of different photonic platforms to achieve new capabilities and functionality not possible using any single platform. These include (a) chip-bonding III-V laser gain media to silicon-on-insulator waveguides (Ref. 87); (b) InAs quantum dots on a silicon oxynitride photonics chip (Ref. 199); (c) GaAs-on-insulator waveguides demonstrating record second-harmonic conversion efficiency  $>46\text{ mW}^{-1}\text{cm}^{-2}$  (Ref. 95); (d) AlGaAs-on-silicon platform for multifunctional integrated photonics in the mid-infrared (Ref. 200); and (e) AlGaAs-on-insulator with  $<0.2\text{ dB/cm}$  propagation loss enabling  $>3 \times 10^6$  resonator Q (Ref. 98). Panel (a) is reproduced with permission from Komljenovic *et al.*, *J. Light. Technol.* **34**, 20 (2016). Copyright 2016 IEEE. Panel (b) is reproduced with permission from Davanco *et al.*, *Nat. Commun.* **8**, 889 (2017). Copyright 2017 Springer Nature Open Access. Panels (c) and (d) are reproduced with permission from Stanton *et al.*, *Opt. Express* **28**, 9521 (2020) and reproduced with permission from Chiles *et al.*, *Optica* **6**, 1246 (2019). Copyright 2019 The Optical Society. Panel (e) is reproduced with permission from Chang *et al.*, *Nat. Commun.* **11**, 1 (2020). Copyright 2020 Springer Nature Open Access.

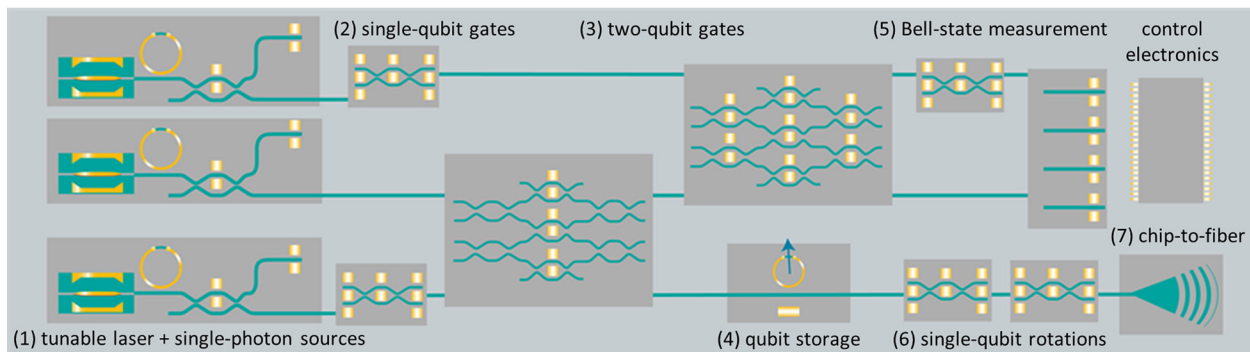


**Fig. 13.** Illustrative example of an all-on-chip QPIC platform for photonic qubit teleportation comprising (1) on-chip tunable lasers pumping nonlinear resonators for generating heralded single-photons that are mapped onto path-encoded qubits, (2) single qubit gates to prepare the target and ancillary qubits, (3) entangling gates, (4) qubit storage elements, (5) projective Bell-state measurements, (6) active feed-forward to perform rotations on the teleported qubit, and (7) chip-to-fiber gratings for chip-to-chip teleportation.

improve upon pump rejection through new filter designs, substrate engineering, and chip-integrated detector optical isolation through shielding.

Another challenge that hinders the integration is the fact that no single material platform exists with the best performance in each metric important for quantum applications. This notion has motivated numerous studies into heterogeneous integration strategies that combine the best of each platform. For example, silicon photonics benefits from the mature CMOS foundry manufacturing process, enabling thousands of photonic components on a single chip, and, thus, holds the promise for high-level integrated quantum circuits and high-volume, low-cost production. On the other hand, III-V semiconductor materials can serve as excellent on-chip pump sources as well as a nonlinear medium for quantum light generation and frequency translation. In particular, the (Al)GaAsOI platform has the highest  $\chi^{(2)}$  and  $\chi^{(3)}$  nonlinearities with recent demonstration of  $Q > 10^6$ ; thus, it may quickly surpass other materials as state-of-the-art for quantum light generation. Both heterogeneous and hybrid integration methods have been developed and applied to quantum applications to bring these different platforms together, several of which are shown in Fig. 12.

The final piece to full system integration on a single chip is the single-photon detector. At present, although waveguide-coupled SNSPDs have been realized with near-unity quantum efficiency, sub-70 ps timing jitter, and sub-mHz dark count rates, these detectors have yet to be integrated at a large scale with quantum photonic chips. The challenge lies with the cryogenic operating temperature of SNSPDs, which are incompatible with power-hungry thermal tuning of photonic components due to the drop in the thermo-optic coefficient. The power dissipated from thermal tuners will also likely heat the entire chip, thus deteriorating SNSPD performance and introducing cross-talk between components. In order to address this problem, novel tuning schemes are required in future quantum applications, such as electro-optic, piezo-optic, or carrier-induced effects. For this purpose, LN, (Al)GaAs, AlN, and 2D materials may serve as excellent candidates. While there are relatively few studies reporting waveguide-integrated single-photon avalanche diodes (SPADs), such detectors would enable possible room-temperature operation of large-scale, fully integrated QPICs. Initial reports in the past few years are promising with Ge-on-Si and InGaAs/Si SPADs with an efficiency of  $\sim 5\%$  and a timing jitter of  $\sim 100$  ps.<sup>201–204</sup> Future studies focusing on material

defect passivation, improving waveguide-detector co-design with gating, and refining heterogeneous integration methods may lead to the necessary reduction in the dark count rate and increase in the single-photon detection efficiency for all-on-chip QPICs operating at room temperature. An exemplary QPIC is shown in Fig. 13 for realizing teleportation of a photonic qubit with active feed-forward control, which is an essential resource for quantum technologies, e.g., photonic quantum information processing or the teleportation of quantum states to separate chips residing at nodes of a quantum network.

## ACKNOWLEDGMENTS

The authors gratefully acknowledge support via the UC Santa Barbara NSF Quantum Foundry funded via the Q-AMASE-i program under Award No. DMR-1906325. G.M. acknowledges support from AFOSR YIP Award No. FA9550-20-1-0150.

## DATA AVAILABILITY

Data sharing is not applicable to this article as no new data were created or analyzed in this study.

## REFERENCES

- <sup>1</sup>J. L. O'Brien, A. Furusawa, and J. Vučković, *Nat. Photonics* **3**, 687 (2009).
- <sup>2</sup>J. C. Howell, R. S. Bennink, S. J. Bentley, and R. W. Boyd, *Phys. Rev. Lett.* **92**, 210403 (2004).
- <sup>3</sup>Z. Y. Ou and Y. J. Lu, *Phys. Rev. Lett.* **83**, 2556 (1999).
- <sup>4</sup>M. Fiorentino, S. M. Spillane, R. G. Beausoleil, T. D. Roberts, P. Battle, and M. W. Munro, *Opt. Express* **15**, 7479 (2007).
- <sup>5</sup>H. Takesue and K. Inoue, *Phys. Rev. A* **70**, 31802 (2004).
- <sup>6</sup>K. Garay-Palmett *et al.*, *Opt. Express* **15**, 14870 (2007).
- <sup>7</sup>A. I. Lvovsky, *Photonics* **1**, 121 (2015).
- <sup>8</sup>J. B. Spring *et al.*, *Opt. Express* **21**, 13522 (2013).
- <sup>9</sup>P. G. Kwiat, K. Mattle, H. Weinfurter, A. Zeilinger, A. V. Sergienko, and Y. Shih, *Phys. Rev. Lett.* **75**, 4337 (1995).
- <sup>10</sup>H. Jayakumar, A. Predojević, T. Kauten, T. Huber, G. S. Solomon, and G. Weihs, *Nat. Commun.* **5**, 4251 (2014).
- <sup>11</sup>F. Samara, A. Martin, C. Autebert, M. Karpov, T. J. Kippenberg, H. Zbinden, and R. Thew, *Opt. Express* **27**, 19309 (2019).
- <sup>12</sup>P. Senellart, G. Solomon, and A. White, *Nat. Nanotechnol.* **12**, 1026 (2017).
- <sup>13</sup>I. Aharonovich, D. Englund, and M. Toth, *Nat. Photonics* **10**, 631 (2016).
- <sup>14</sup>E. Meyer-Scott, C. Silberhorn, and A. Miggall, *Rev. Sci. Instrum.* **91**, 041101 (2020).
- <sup>15</sup>M. J. Collins *et al.*, *Nat. Commun.* **4**, 2582 (2013).

- <sup>16</sup>R. B. Jin *et al.*, *Sci. Rep.* **4**, 7468 (2014).
- <sup>17</sup>P. Sibson *et al.*, *Nat. Commun.* **8**, 13984 (2017).
- <sup>18</sup>P. Kok, W. J. Munro, K. Nemoto, T. C. Ralph, J. P. Dowling, and G. J. Milburn, *Rev. Mod. Phys.* **79**, 135 (2007).
- <sup>19</sup>S. D. Huver, C. F. Wildfeuer, and J. P. Dowling, *Phys. Rev. A* **78**, 63828 (2008).
- <sup>20</sup>J. Aasi *et al.*, *Nat. Photonics* **7**, 613 (2013).
- <sup>21</sup>F. Acerneze *et al.*, *Phys. Rev. Lett.* **123**, 231108 (2019).
- <sup>22</sup>M. Giustina *et al.*, 250401, 1 (2015).
- <sup>23</sup>L. K. Shalm *et al.*, *Phys. Rev. Lett.* **115**, 250402 (2015).
- <sup>24</sup>N. Chandra and H. Prakash, *Phys. Rev. A* **1**, 1696 (1970).
- <sup>25</sup>J. F. Clauser and A. Shimony, *Rep. Prog. Phys.* **41**, 1881 (1978).
- <sup>26</sup>C. Monroe, D. M. Meekhof, B. E. King, W. M. Itano, and D. J. Wineland, *Phys. Rev. Lett.* **75**, 4714 (1995).
- <sup>27</sup>A. Politi, M. J. Cryan, J. G. Rarity, S. Yu, and J. L. O'Brien, *Science* **320**, 646 (2008).
- <sup>28</sup>D. Bonneau *et al.*, *New J. Phys.* **14**, 045003 (2012).
- <sup>29</sup>J. Wang *et al.*, *Science* **360**, 285 (2018).
- <sup>30</sup>X. Qiang *et al.*, *Nat. Photonics* **12**, 534 (2018).
- <sup>31</sup>J. W. Silverstone *et al.*, *Nat. Photonics* **8**, 104 (2014).
- <sup>32</sup>A. Politi, J. C. F. Matthews, and J. L. O'Brien, *Science* **325**, 1221 (2009).
- <sup>33</sup>A. Peruzzo *et al.*, *Science* **329**, 1500 (2010).
- <sup>34</sup>P. J. Shadbolt, M. R. Verde, A. Peruzzo, A. Politi, A. Laing, M. Lobino, J. C. F. Matthews, M. G. Thompson, and J. L. O'Brien, *Nat. Photonics* **6**, 45 (2012).
- <sup>35</sup>T. Gerrits *et al.*, *Phys. Rev. A* **84**, 060301 (2011).
- <sup>36</sup>M. Arcari *et al.*, *Phys. Rev. Lett.* **113**, 093603 (2014).
- <sup>37</sup>A. Crespi *et al.*, *Nat. Photonics* **7**, 545 (2013).
- <sup>38</sup>M. Tillmann, B. Dakić, R. Heilmann, S. Nolte, A. Szameit, and P. Walther, *Nat. Photonics* **7**, 540 (2013).
- <sup>39</sup>J. B. Spring *et al.*, *Science* **339**, 798 (2013).
- <sup>40</sup>J. Carolan *et al.*, *Nat. Photonics* **8**, 621 (2014).
- <sup>41</sup>M. A. Broome, A. Fedrizzi, S. Rahimi-Keshari, J. Dove, S. Aaronson, T. C. Ralph, and A. G. White, *Science* **339**, 794 (2013).
- <sup>42</sup>J. Wang *et al.*, *Optica* **3**, 407 (2016).
- <sup>43</sup>J. Carolan *et al.*, *Science* **349**, 711 (2015).
- <sup>44</sup>M. Bentivegna *et al.*, *Sci. Adv.* **1**, e1400255 (2015).
- <sup>45</sup>M. A. Ciampini, A. Orioux, S. Paesani, F. Sciarrino, G. Corrielli, A. Crespi, R. Ramponi, R. Osellame, and P. Mataloni, *Light* **5**, e16064 (2016).
- <sup>46</sup>J. B. Spring *et al.*, *Optica* **4**, 90 (2017).
- <sup>47</sup>J. C. Adcock, C. Vigliar, R. Santagati, J. W. Silverstone, and M. G. Thompson, *Nat. Commun.* **10**, 3528 (2019).
- <sup>48</sup>S. Paesani *et al.*, *Nat. Phys.* **15**, 925 (2019).
- <sup>49</sup>N. H. Wan *et al.*, *Nature* **583**, 226 (2020).
- <sup>50</sup>T. Heindel *et al.*, *New J. Phys.* **14**, 083001 (2012).
- <sup>51</sup>H. Wang *et al.*, *Phys. Rev. Lett.* **123**, 250503 (2019).
- <sup>52</sup>J. Zhao, C. Ma, M. Rüsing, and S. Mookherjea, *Phys. Rev. Lett.* **124**, 163603 (2020).
- <sup>53</sup>L. Chang *et al.*, *Laser Photonics Rev.* **12**, 1800149 (2018).
- <sup>54</sup>K. Zielnicki, K. Garay-Palmett, D. Cruz-Delgado, H. Cruz-Ramirez, M. F. O'Boyle, B. Fang, V. O. Lorenz, A. B. U'Ren, and P. G. Kwiat, *J. Mod. Opt.* **65**, 1141 (2018).
- <sup>55</sup>R. Kumar, J. R. Ong, M. Savanier, and S. Mookherjea, *Nat. Commun.* **5**, 5489 (2014).
- <sup>56</sup>J. Sperling and W. Vogel, *Phys. Scr.* **83**, 045002 (2011).
- <sup>57</sup>B. M. Terhal and P. Horodecki, *Phys. Rev. A* **61**, 40301 (2000).
- <sup>58</sup>J. B. Pors, S. S. R. Oemrawsingh, A. Aiello, M. P. van Exter, E. R. Eliel, G. W. 't Hooft, and J. P. Woerdman, *Phys. Rev. Lett.* **101**, 120502 (2008).
- <sup>59</sup>A. L. Gaeta, M. Lipson, and T. J. Kippenberg, *Nat. Photonics* **13**, 158 (2019).
- <sup>60</sup>D. Thomson *et al.*, *J. Opt.* **18**, 073003 (2016).
- <sup>61</sup>M. Tran, D. Huang, T. Komljenovic, J. Peters, A. Malik, and J. Bowers, *Appl. Sci.* **8**, 1139 (2018).
- <sup>62</sup>S. Paesani, M. Borghi, S. Signorini, A. Maiños, L. Pavesi, and A. Laing, *Nat. Commun.* **11**, 2505 (2020).
- <sup>63</sup>A. G. Griffith *et al.*, *Nat. Commun.* **6**, 6299 (2015).
- <sup>64</sup>C. Xiang, W. Jin, J. Guo, C. Williams, A. Netherton, L. Chang, P. Morton, and J. Bowers, *Opt. Express* **28**, 19926 (2020).
- <sup>65</sup>B. Korzh *et al.*, *Nat. Photonics* **14**, 250 (2020).
- <sup>66</sup>E. A. Dauler, M. E. Grein, A. J. Kerman, F. Marsili, S. Miki, S. W. Nam, M. D. Shaw, H. Terai, V. B. Verma, and T. Yamashita, *Opt. Eng.* **53**, 081907 (2014).
- <sup>67</sup>V. B. Verma *et al.*, *Appl. Phys. Lett.* **105**, 122601 (2014).
- <sup>68</sup>G. T. Reed, G. Mashanovich, F. Y. Gardes, and D. J. Thomson, *Nat. Photonics* **4**, 518 (2010).
- <sup>69</sup>M. H. P. Pfeiffer, J. Liu, A. S. Raja, T. Morais, B. Ghadiani, and T. J. Kippenberg, *Optica* **5**, 884 (2018).
- <sup>70</sup>J. Liu, G. Huang, R. N. Wang, J. He, A. S. Raja, T. Liu, N. J. Engelsen, and T. J. Kippenberg, "High-yield wafer-scale fabrication of ultralow-loss, dispersion-engineered silicon nitride photonic circuits," *arXiv:2005.13949*.
- <sup>71</sup>X. Ji, F. A. S. Barbosa, S. P. Roberts, A. Dutt, J. Cardenas, Y. Okawachi, A. Bryant, A. L. Gaeta, and M. Lipson, *Optica* **4**, 619 (2017).
- <sup>72</sup>C. Monroe and J. Kim, *Science* **339**, 1164 LP (2013).
- <sup>73</sup>X. Lu *et al.*, *Nat. Photonics* **13**, 593 (2019).
- <sup>74</sup>X. Lu, Q. Li, D. A. Westly, G. Moille, A. Singh, V. Anant, and K. Srinivasan, *Nat. Phys.* **15**, 373 (2019).
- <sup>75</sup>A. Arbabi and L. L. Goddard, *Opt. Lett.* **38**, 3878 (2013).
- <sup>76</sup>E. L. Wooten *et al.*, *IEEE J. Sel. Top. Quantum Electron.* **6**, 69 (2000).
- <sup>77</sup>L. Chang, Y. Li, N. Volet, L. Wang, J. Peters, and J. E. Bowers, *Optica* **3**, 531 (2016).
- <sup>78</sup>C. Wang, M. Zhang, X. Chen, M. Bertrand, A. Shams-Ansari, S. Chandrasekhar, P. Winzer, and M. Lončar, *Nature* **562**, 101 (2018).
- <sup>79</sup>Y. Qi and Y. Li, *Nanophotonics* **9**, 1287 (2020).
- <sup>80</sup>M. Zhang, C. Wang, R. Cheng, A. Shams-Ansari, and M. Lončar, *Optica* **4**, 1536 (2017).
- <sup>81</sup>B. Desiatov, A. Shams-Ansari, M. Zhang, C. Wang, and M. Lončar, *Optica* **6**, 380 (2019).
- <sup>82</sup>C. Wang, M. Zhang, M. Yu, R. Zhu, H. Hu, and M. Loncar, *Nat. Commun.* **10**, 1 (2019).
- <sup>83</sup>Y. He, Q.-F. Yang, J. Ling, R. Luo, H. Liang, M. Li, B. Shen, H. Wang, K. Vahala, and Q. Lin, *Optica* **6**, 1138 (2019).
- <sup>84</sup>J. Lu, J. B. Surya, X. Liu, A. W. Bruch, Z. Gong, Y. Xu, and H. X. Tang, *Optica* **6**, 1455 (2019).
- <sup>85</sup>L. Shao *et al.*, *Optica* **6**, 1498 (2019).
- <sup>86</sup>M. Yu, Y. Okawachi, R. Cheng, C. Wang, M. Zhang, A. L. Gaeta, and M. Lončar, *Light* **9**, 1 (2020).
- <sup>87</sup>T. Komljenovic *et al.*, *J. Lightwave Technol.* **34**, 20 (2016).
- <sup>88</sup>J. C. Norman *et al.*, *IEEE J. Quantum Electron.* **55**, 2000511 (2019).
- <sup>89</sup>A. W. Fang, H. Park, O. Cohen, R. Jones, M. J. Paniccia, and J. E. Bowers, *Opt. Express* **14**, 9203 (2006).
- <sup>90</sup>A. Y. Liu and J. Bowers, *IEEE J. Sel. Top. Quantum Electron.* **24**, 6000412 (2018).
- <sup>91</sup>C. McDonald, G. Moody, S. W. Nam, R. P. Mirin, J. M. Shainline, A. McCaughan, S. Buckley, and K. L. Silverman, *Appl. Phys. Lett.* **115**, 081105 (2019).
- <sup>92</sup>C. Xiong, W. H. P. Pernice, and H. X. Tang, *Nano Lett.* **12**, 3562 (2012).
- <sup>93</sup>C. Xiong, W. Pernice, K. K. Ryu, C. Schuck, K. Y. Fong, T. Palacios, and H. X. Tang, *Opt. Express* **19**, 10462 (2011).
- <sup>94</sup>X. Guo, C. Zou, C. Schuck, H. Jung, R. Cheng, and H. X. Tang, *Light* **6**, e16249 (2017).
- <sup>95</sup>E. J. Stanton, J. Chiles, N. Nader, G. Moody, N. Volet, L. Chang, J. E. Bowers, S. Woo Nam, and R. P. Mirin, *Opt. Express* **28**, 9521 (2020).
- <sup>96</sup>M. Pu, L. Ottaviano, E. Semenova, and K. Vynd, *Optica* **3**, 823 (2016).
- <sup>97</sup>D. J. Wilson, K. Schneider, S. Hönl, M. Anderson, Y. Baumgartner, L. Czornomaz, T. J. Kippenberg, and P. Seidler, *Nat. Photonics* **14**, 57 (2020).
- <sup>98</sup>L. Chang *et al.*, *Nat. Commun.* **11**, 3464 (2020).
- <sup>99</sup>W. Xie, L. Chang, H. Shu, J. C. Norman, J. D. Peters, X. Wang, and J. E. Bowers, "Ultrahigh-Q AlGaAs-on-insulator microresonators for integrated nonlinear photonics," *arXiv:2004.14537*.
- <sup>100</sup>B. Guha *et al.*, *Optica* **4**, 218 (2017).
- <sup>101</sup>X. Liu, A. W. Bruch, Z. Gong, J. Lu, J. B. Surya, L. Zhang, J. Wang, J. Yan, and H. X. Tang, *Optica* **5**, 1279 (2018).
- <sup>102</sup>A. Y. Liu, C. Zhang, J. Norman, A. Snyder, D. Lubyshev, J. M. Fastenau, A. W. K. Liu, A. C. Gossard, and J. E. Bowers, *Appl. Phys. Lett.* **104**, 041104 (2014).
- <sup>103</sup>K. Y. Yang, D. Y. Oh, S. H. Lee, Q.-F. Yang, X. Yi, B. Shen, H. Wang, and K. Vahala, *Nat. Photonics* **12**, 297 (2018).

- <sup>104</sup>H. Jung *et al.*, *Nonlinear Optics* (OSA, Washington, DC, 2019), p. NW2A.3.
- <sup>105</sup>X. Liu *et al.*, *Opt. Express* **25**, 587 (2017).
- <sup>106</sup>M. Gündry, K. Yang, D. Lukin, A. Markosyan, J. Yang, M. Fejer, and J. Vuckovic, *Optica* **7**, 1139 (2020).
- <sup>107</sup>A. Biberman, M. J. Shaw, E. Timurdogan, J. B. Wright, and M. R. Watts, *Opt. Lett.* **37**, 4236 (2012).
- <sup>108</sup>R. R. Kumar, M. Raevskia, V. Pogoretskii, Y. Jiao, and H. K. Tsang, *Appl. Phys. Lett.* **114**, 021104 (2019).
- <sup>109</sup>J. Zeuner, A. N. Sharma, M. Tillmann, R. Heilmann, M. Gräfe, A. Moqanaki, A. Szameit, and P. Walther, *npj Quantum Inf.* **4**, 13 (2018).
- <sup>110</sup>A. M. Brańczyk, T. C. Ralph, W. Helwig, and C. Silberhorn, *New J. Phys.* **12**, 063001 (2010).
- <sup>111</sup>D. Llewellyn *et al.*, *Nat. Phys.* **16**, 148 (2020).
- <sup>112</sup>Z. Vernon, M. Liscidini, and J. E. Sipe, *Opt. Lett.* **41**, 788 (2016).
- <sup>113</sup>Z. Vernon *et al.*, *Opt. Lett.* **42**, 3638 (2017).
- <sup>114</sup>Y. Liu *et al.*, *Opt. Lett.* **45**, 73 (2020).
- <sup>115</sup>B. Burridge, I. I. Faruque, J. Rarity, and J. Barreto, "High spectro-temporal purity single-photons from silicon micro-racetrack resonators using a dual-pulse configuration," *Opt. Lett.* **45**, 4048 (2020).
- <sup>116</sup>I. Aharonovich, D. Englund, and M. Toth, *Nat. Photonics* **10**, 631 (2016).
- <sup>117</sup>N. Somaschi, V. Giesz, L. De Santis, J. C. Loredo, M. P. Almeida, G. Hornecker, S. L. Portolupi, T. Grange, C. Antón, J. Demory, C. Gómez, I. Sagnes, N. D. Lanzillotti-Kimura, A. Lemaitre, A. Auffeves, A. G. White, L. Lanco, and P. Senellart, *Nat. Photonics* **10**, 340 (2016).
- <sup>118</sup>P. Senellart, G. Solomon, and A. White, *Nat. Nanotechnol.* **12**, 1026 (2017).
- <sup>119</sup>H. Wang *et al.*, *Nat. Photonics* **13**, 770 (2019).
- <sup>120</sup>Y. Arakawa and M. J. Holmes, *Appl. Phys. Rev.* **7**, 021309 (2020).
- <sup>121</sup>X. Ding *et al.*, *Phys. Rev. Lett.* **116**, 020401 (2016).
- <sup>122</sup>S. Unsleber *et al.*, *Opt. Express* **24**, 8539 (2016).
- <sup>123</sup>M. J. Holmes, M. Arita, and Y. Arakawa, *Semicond. Sci. Technol.* **34**, 033001 (2019).
- <sup>124</sup>S. Tamariz, G. Callsen, J. Stachurski, K. Shojiki, R. Butté, and N. Grandjean, *ACS Photonics* **7**, 1515 (2020).
- <sup>125</sup>M. J. Holmes, K. Choi, S. Kako, M. Arita, and Y. Arakawa, *Nano Lett.* **14**, 982 (2014).
- <sup>126</sup>X. He, H. Htoon, S. K. Doorn, W. H. P. Pernice, F. Pyatkov, R. Krupke, A. Jeantet, Y. Chassagneux, and C. Voisin, *Nat. Mater.* **17**, 663 (2018).
- <sup>127</sup>X. He *et al.*, *Nat. Photonics* **11**, 577 (2017).
- <sup>128</sup>S. Castelletto, F. A. Inam, S. Sato, and A. Boretti, *Beilstein J. Nanotechnol.* **11**, 740 (2020).
- <sup>129</sup>T. T. Tran, K. Bray, M. J. Ford, M. Toth, and I. Aharonovich, *Nat. Nanotechnol.* **11**, 37 (2016).
- <sup>130</sup>Y. M. He *et al.*, *Nat. Nanotechnol.* **10**, 497 (2015).
- <sup>131</sup>S. Kumar, A. Kaczmarczyk, and B. D. Gerardot, *Nano Lett.* **15**, 7567 (2015).
- <sup>132</sup>Y. M. He, G. Clark, J. R. Schaibley, Y. He, M. C. Chen, Y. J. Wei, X. Ding, Q. Zhang, W. Yao, X. Xu, C. Y. Lu, and J. W. Pan, *Nat. Nanotechnol.* **10**, 497 (2015).
- <sup>133</sup>T. Schröder, F. Gädke, M. J. Banholzer, and O. Benson, *New J. Phys.* **13**, 055017 (2011).
- <sup>134</sup>E. Neu, D. Steinmetz, J. Riedrich-Möller, S. Gsell, M. Fischer, M. Schreck, and C. Becher, *New J. Phys.* **13**, 025012 (2011).
- <sup>135</sup>S. Castelletto, B. C. Johnson, V. Ivády, N. Stavrias, T. Umeda, A. Gali, and T. Ohshima, *Nat. Mater.* **13**, 151 (2014).
- <sup>136</sup>A. J. Morfa, B. C. Gibson, M. Karg, T. J. Karle, A. D. Greentree, P. Mulvaney, and S. Tomljenovic-Hanic, *Nano Lett.* **12**, 949 (2012).
- <sup>137</sup>P. Siyushev, K. Xia, R. Reuter, M. Jamali, N. Zhao, N. Yang, C. Duan, N. Kukharchyk, A. D. Wieck, R. Kolesov, and J. Wrachtrup, *Nat. Commun.* **5**, 1 (2014).
- <sup>138</sup>C. Reimer *et al.*, *Opt. Express* **22**, 6535 (2014).
- <sup>139</sup>C. Ma, X. Wang, V. Anant, A. D. Beyer, M. D. Shaw, and S. Mookherjea, *Opt. Express* **25**, 32995 (2017).
- <sup>140</sup>S. Ramelow, A. Farsi, S. Clemmen, D. Orquiza, K. Luke, M. Lipson, and A. L. Gaeta, *arXiv:1508.04358* (2015).
- <sup>141</sup>M. Förtsch, J. U. Fürst, C. Wittmann, D. Strekalov, A. Aiello, M. V. Chekhova, C. Silberhorn, G. Leuchs, and C. Marquardt, *Nat. Commun.* **4**, 1 (2013).
- <sup>142</sup>L. Olislager, J. Cussey, A. T. Nguyen, P. Emplit, S. Massar, J.-M. Merolla, and K. P. Huy, *Phys. Rev. A* **82**, 13804 (2010).
- <sup>143</sup>D. Grassani, S. Azzini, M. Liscidini, M. Galli, M. J. Strain, M. Sorel, J. E. Sipe, and D. Bajoni, *Optica* **2**, 88 (2015).
- <sup>144</sup>D. F. V. James, P. G. Kwiat, W. J. Munro, and A. G. White, *Phys. Rev. A* **64**, 52312 (2001).
- <sup>145</sup>L. T. Feng *et al.*, *npj Quantum Inf.* **5**, 2 (2019).
- <sup>146</sup>A. S. Solntsev and A. A. Sukhorukov, *Rev. Phys.* **2**, 19 (2017).
- <sup>147</sup>P. Imany, J. A. Jaramillo-Villegas, O. D. Odele, K. Han, D. E. Leaird, J. M. Lukens, P. Lougovski, M. Qi, and A. M. Weiner, *Opt. Express* **26**, 1825 (2018).
- <sup>148</sup>J. B. Altepeter, E. R. Jeffrey, and P. G. Kwiat, *Adv. At. Mol. Opt. Phys.* **52**, 105 (2005).
- <sup>149</sup>N. Gisin, G. Ribordy, W. Tittel, and H. Zbinden, *Rev. Mod. Phys.* **74**, 145 (2002).
- <sup>150</sup>I. Marcikic, H. De Riedmatten, W. Tittel, H. Zbinden, M. Legré, and N. Gisin, *Phys. Rev. Lett.* **93**, 180502 (2004).
- <sup>151</sup>J. Mower, Z. Zhang, P. Desjardins, C. Lee, J. H. Shapiro, and D. Englund, *Phys. Rev. A* **87**, 62322 (2013).
- <sup>152</sup>J. D. Franson, *Phys. Rev. Lett.* **62**, 2205 (1989).
- <sup>153</sup>P. Sarrafi, E. Y. Zhu, K. Dolgaleva, B. M. Holmes, D. C. Hutchings, J. S. Aitchison, and L. Qian, *Appl. Phys. Lett.* **103**, 251115 (2013).
- <sup>154</sup>M. A. Taylor, J. Janousek, V. Daria, J. Knittel, B. Hage, H. A. Bachor, and W. P. Bowen, *Nat. Photonics* **7**, 229 (2013).
- <sup>155</sup>P. H. S. Ribeiro, C. Schwob, A. Maitre, and C. Fabre, *Opt. Lett.* **22**, 1893 (1997).
- <sup>156</sup>V. Giovannetti, S. Lloyd, and L. Maccone, *Science* **306**, 1330 LP (2004).
- <sup>157</sup>E. S. Polzik, J. Carri, and H. J. Kimble, *Phys. Rev. Lett.* **68**, 3020 (1992).
- <sup>158</sup>S. L. Braunstein and P. van Loock, *Rev. Mod. Phys.* **77**, 513 (2005).
- <sup>159</sup>R. E. Slusher, L. W. Hollberg, B. Yurke, J. C. Mertz, and J. F. Valley, *Phys. Rev. Lett.* **55**, 2409 (1985).
- <sup>160</sup>J. U. Fürst, D. V. Strekalov, D. Elser, A. Aiello, U. L. Andersen, C. Marquardt, and G. Leuchs, *Phys. Rev. Lett.* **106**, 113901 (2011).
- <sup>161</sup>A. H. Safavi-Naeini, S. Gröblacher, J. T. Hill, J. Chan, M. Aspelmeyer, and O. Painter, *Nature* **500**, 185 (2013).
- <sup>162</sup>A. Dutt, S. Miller, K. Luke, A. L. Gaeta, P. Nussenzveig, and M. Lipson, *Opt. Lett.* **41**, 223 (2016).
- <sup>163</sup>A. Dutt, K. Luke, S. Manipatruni, A. L. Gaeta, P. Nussenzveig, and M. Lipson, *Phys. Rev. Appl.* **3**, 044005 (2015).
- <sup>164</sup>Y. Eto, A. Koshio, A. Ohshiro, J. Sakurai, K. Horie, T. Hirano, and M. Sasaki, *Opt. Lett.* **36**, 4653 (2011).
- <sup>165</sup>H. Vahlbruch, M. Mehmet, K. Danzmann, and R. Schnabel, *Phys. Rev. Lett.* **117**, 110801 (2016).
- <sup>166</sup>Y. Zhao, Y. Okawachi, J. K. Jang, X. Ji, M. Lipson, and A. L. Gaeta, *Phys. Rev. Lett.* **124**, 193601 (2020).
- <sup>167</sup>F. Mondain, T. Lunghi, A. Zavatta, E. Gouzien, F. Doutre, M. De Micheli, S. Tanzilli, and V. D'Auria, *Photonics Res.* **7**, A36 (2019).
- <sup>168</sup>T. Kashiwazaki, N. Takanashi, T. Yamashima, T. Kazama, K. Enbusu, R. Kasahara, T. Umeki, and A. Furusawa, *APL Photonics* **5**, 036104 (2020).
- <sup>169</sup>A. M. Fox, B. Huttner, and J. F. Ryan, *Phys. Rev. A* **50**, 4415 (1994).
- <sup>170</sup>Y. Zhang, M. Menotti, K. Tan, V. D. Vaidya, D. H. Mahler, L. Zatti, M. Liscidini, B. Morrison, and Z. Vernon, "Single-mode quadrature squeezing using dual-pump four-wave mixing in an integrated nanophotonic device," *arXiv:2001.09474*.
- <sup>171</sup>S. Lorenz, C. Silberhorn, N. Korolkova, R. S. Windeler, and G. Leuchs, *Appl. Phys. B* **73**, 855 (2001).
- <sup>172</sup>J. Milanovic, A. Huck, J. Heersink, C. Marquardt, U. L. Andersen, and G. Leuchs, *Laser Phys.* **17**, 559 (2007).
- <sup>173</sup>P. K. Lam, T. C. Ralph, B. C. Buchler, D. E. McClelland, H. A. Bachor, and J. Gao, *J. Opt. B*, 469 (1999).
- <sup>174</sup>A. M. Fox, J. J. Baumberg, M. Dabbicco, B. Huttner, and J. F. Ryan, *Phys. Rev. Lett.* **74**, 1728 (1995).
- <sup>175</sup>T. Eberle, S. Steinlechner, J. Bauchrowitz, V. Händchen, H. Vahlbruch, M. Mehmet, H. Müller-Ebhardt, and R. Schnabel, *Phys. Rev. Lett.* **104**, 251102 (2010).
- <sup>176</sup>G.-M. Schucan, A. M. Fox, and J. F. Ryan, *Opt. Lett.* **23**, 712 (1998).
- <sup>177</sup>D. Awschalom *et al.*, "Development of quantum interConnects (QuICs) for next-generation information technologies," *arXiv:1912.06642*.
- <sup>178</sup>A. Singh, Q. Li, J. Liu, X. Lu, C. Schneider, and K. Srinivasan, *Optica* **6**, 563 (2019).

- <sup>179</sup>C. Wang, C. Langrock, A. Marandi, M. Jankowski, M. Zhang, B. Desiatov, M. M. Fejer, and M. Lončar, *Optica* **5**, 1438 (2018).
- <sup>180</sup>X. Liu, B. Kuyken, G. Roelkens, R. Baets, R. M. Osgood, and W. M. J. Green, *Nat. Photonics* **6**, 667 (2012).
- <sup>181</sup>Q. Li, M. Davanco, and K. Srinivasan, *Nat. Photonics* **10**, 406 (2016).
- <sup>182</sup>D. P. Lake, M. Mitchell, H. Jayakumar, L. F. Dos Santos, D. Curic, and P. E. Barclay, *Appl. Phys. Lett.* **108**, 031109 (2016).
- <sup>183</sup>X. Guo, C.-L. Zou, and H. X. Tang, *Optica* **3**, 1126 (2016).
- <sup>184</sup>P. Imany, J. A. Jaramillo-Villegas, M. S. Alshaykh, J. M. Lukens, O. D. Odele, A. J. Moore, D. E. Leaird, M. Qi, and A. M. Weiner, *npj Quantum Inf.* **5**, 59 (2019).
- <sup>185</sup>X. Guo, C. L. Zou, H. Jung, and H. X. Tang, *Phys. Rev. Lett.* **117**, 123902 (2016).
- <sup>186</sup>R. Luo, Y. He, H. Liang, M. Li, J. Ling, and Q. Lin, *Phys. Rev. Appl.* **11**, 034026 (2019).
- <sup>187</sup>L. Chang *et al.*, 31st Annual Conference on IEEE Photonics Society (IPC) (2018).
- <sup>188</sup>A. W. Bruch, X. Liu, X. Guo, J. B. Surya, Z. Gong, L. Zhang, J. Wang, J. Yan, and H. X. Tang, *Appl. Phys. Lett.* **113**, 131102 (2018).
- <sup>189</sup>J. Lin, Y. Xu, J. Ni, M. Wang, Z. Fang, L. Qiao, W. Fang, and Y. Cheng, *Phys. Rev. Appl.* **6**, 014002 (2016).
- <sup>190</sup>X. Zhang, Q. T. Cao, Z. Wang, Y. xi Liu, C. W. Qiu, L. Yang, Q. Gong, and Y. F. Xiao, *Nat. Photonics* **13**, 21 (2019).
- <sup>191</sup>J. U. Fürst, D. V. Strekalov, D. Elser, M. Lassen, U. L. Andersen, C. Marquardt, and G. Leuchs, *Phys. Rev. Lett.* **104**, 153901 (2010).
- <sup>192</sup>V. S. Ilchenko, A. A. Savchenkov, A. B. Matsko, and L. Maleki, *Phys. Rev. Lett.* **92**, 4 (2004).
- <sup>193</sup>D. Grassani, M. H. P. Pfeiffer, T. J. Kippenberg, and C.-S. Brès, *Opt. Lett.* **44**, 106 (2019).
- <sup>194</sup>A. Chowdhury, H. M. Ng, M. Bhardwaj, and N. G. Weimann, *Appl. Phys. Lett.* **83**, 1077 (2003).
- <sup>195</sup>S. May, M. Kues, M. Clerici, and M. Sorel, *Opt. Lett.* **44**, 1339 (2019).
- <sup>196</sup>B. J. Metcalf *et al.*, *Nat. Photonics* **8**, 770 (2014).
- <sup>197</sup>S. Buckley, J. Chiles, A. N. McCaughan, G. Moody, K. L. Silverman, M. J. Stevens, R. P. Mirin, S. W. Nam, and J. M. Shainline, *Appl. Phys. Lett.* **111**, 141101 (2017).
- <sup>198</sup>C. Schuck, W. H. P. Pernice, and H. X. Tang, *Sci. Rep.* **3**, 1893 (2013).
- <sup>199</sup>J.-H. Kim, S. Aghaeimeibodi, J. Carolan, D. Englund, and E. Waks, *Optica* **7**, 291 (2020).
- <sup>200</sup>J. Chiles *et al.*, *Optica* **6**, 1246 (2019).
- <sup>201</sup>N. J. D. Martinez, M. Gehl, C. T. Derose, A. L. Starbuck, A. T. Pomerene, A. L. Lentine, D. C. Trotter, and P. S. Davids, *Opt. Express* **25**, 16130 (2017).
- <sup>202</sup>J. J. Ackert, A. S. Karar, D. J. Paez, P. E. Jessop, J. C. Cartledge, and A. P. Knights, *Opt. Express* **21**, 19530 (2013).
- <sup>203</sup>R. A. Soref, F. De Leonardi, and V. M. N. Passaro, *ACS Appl. Nano Mater.* **2**, 7503 (2019).
- <sup>204</sup>Y. Kang, Y.-H. Lo, M. Bitter, S. Kristjansson, Z. Pan, and A. Pauchard, *Appl. Phys. Lett.* **85**, 1668 (2004).